

**Design and Evaluation of a Clinical Organ-Targeted Positron Emission Tomography  
Camera**

By

Brandon Baldassi

A thesis

Presented to Lakehead University

In partial fulfillment of the requirement for the degree of

Master of Science in Physics

Thunder Bay, Ontario, Canada

© Brandon Baldassi 2023

## Abstract

Positron Emission Tomography (PET) is a non-invasive medical imaging technique which uses radioactive tracers to visualize the metabolic or biochemical function of tissues and organs. PET imaging aids in the accurate diagnosis and management of disease including neurodegeneration and cancer. Standard clinical practice uses whole-body (WB) PET technology which is limited in its ability to detect small lesions due to inadequate spatial resolution and the need for high radiotracer doses due to low sensitivity. This has prompted the development of organ-targeted PET, which places limited field-of-view (FOV) detectors near to an organ for imaging. This approach offers distinct advantages over WB PET, including improved spatial resolution for lesion detection, greater sensitivity for imaging with lower radiotracer doses, and contrast recovery capabilities which permit accurate quantification of radiotracer uptake in small structures.

To realize the potential of organ-targeted PET, a scanner must maximize radiotracer detection sensitivity and accurately reconstruct contrast in small structures. The key to improving PET detection sensitivity lies in the scanner geometry and technological advancements in PET sensors. The organ-targeted PET technology presented in this Thesis uses high-performing solid-state PET sensors seamlessly arranged in a planar geometry to provide complete FOV coverage for the organ under investigation. The technology employs high-yield scintillation crystals, high-gain solid-state photodetectors, adjustable detector temperature control, and specialized acquisition electronics. Developed in Reznik's lab at Lakehead University and the Thunder Bay Regional Health Research Institute (TBRHRI), the technology has been licensed to Radialis Inc., a joint spin-off company of Lakehead University and TBRHRI. Radialis Inc. has optimized the technology for functional breast cancer imaging, resulting in the development and fabrication of the Radialis PET Camera. The imaging performance of Radialis PET camera was evaluated using standardized phantom procedures and compared with other clinical devices. The results indicate unprecedented sensitivity and improved contrast recovery capabilities, and subsequent clinical study has shown that the Radialis PET technology can identify a variety of cancers, even at a 10-fold dose reduction, and reveal clinical details which are not visible with commercial WB PET scanners. It also shows the ability to accurately quantify radiotracer uptake in breast lesions and reconstruct the 3-D volume corresponding to abnormally metabolic tissue.

While standardized measurements can permit a direct comparison between different PET devices, the clinical utility of an organ-targeted PET device cannot be defined solely based on these measurements. The results presented here show that recovery coefficient measured for different lesion sizes and activity concentrations is necessary to define the capabilities of a PET system targeting small lesion detection, size assessment, and activity uptake quantification. Subsequent investigations will inform corrective strategies which can further improve contrast recovery and continue to expand the clinical utility of organ-targeted PET.

Overall, this Thesis demonstrates that the organ-targeted PET technology presented here is a significant technological advancement in maximizing PET detection sensitivity and accurately reconstructing uptake of a radiopharmaceutical in small structures. This breakthrough has immense potential in unlocking new frontiers in early disease diagnosis and treatment assessment for a wide range of medical conditions, including cancer, cardiovascular disease, and neurological disorders.

## **Acknowledgments**

I would like to acknowledge my supervisor, Dr. Alla Reznik, for providing guidance, instruction, and inspiration throughout my graduate studies. I am thankful for her contributions to my education and to my development as a scientist, both of which have been significant. I would also like to acknowledge Dr. Oleksandr Bubon for his support and technical insights which have deepened my understanding of physics in positron emission tomography. In addition, I thank my supervisory committee, Dr. Mitchell Albert and Dr. Apichart Linhananta, for their contributions to my graduate studies.

I would like to recognize members of the Reznik lab, both past and present, who each contribute to the environment for learning and sense of community in our lab. I am grateful for all the experiences we have shared in research and in life. In addition, I would like to acknowledge Mr. William Main and Mr. Terry Wood for inspiring the scientific curiosity in me. Because of them, I will be a student for life. Finally, I thank my family for their ongoing support and continued belief in me. I am indebted to them for all that they have done to allow me opportunities such as this.

## Table of Contents

Design and Evaluation of a Clinical Organ-Targeted Positron Emission Tomography Camera	i
Abstract	ii
Acknowledgments	iv
Table of Contents	v
<b>1. Introduction</b>	<b>1</b>
1.1. Principles of PET Imaging	1
1.1.1. Radioactive Decay and Positron Emission	2
1.1.1. Positron Range and Annihilation	3
1.2. Photon Detection	4
1.1.2. 511 keV Photon Interactions in Matter	4
1.2.1. Photoelectric Interaction	5
1.2.2. Compton Scattering	5
1.2.3. Interaction Cross-Section in Matter	7
1.2.4. Detection of annihilation radiation in PET imaging	8
1.2.5. Noncollinearity	10
1.3. Scintillation Material	10
1.4. Photosensors	11
<b>2. Design of an Organ-Targeted PET Camera</b>	<b>15</b>
2.1. Introduction	15
2.2. High-Performance PET Detector Technology	16
2.2.1. Radialis Organ-Targeted PET Detector and System Design	21
2.2.2. Cooling	22
2.3. Data Acquisition	23
2.3.1. Analog to Digital Conversion	23
1.1.3. Coincidence detection	24
2.3.2. DAQ Event Processing	25
2.3.3. Computer System and Data Storage	25
2.4. Image Reconstruction	26
2.4.1. Reconstruction Algorithm	26
2.5. PET Data Integrity	28
2.5.1. Energy Filter	28

2.5.2.	Angular Filter	29
2.5.3.	Attenuation Correction	29
2.5.4.	Scatter Correction	30
3.	Standardized Imaging Evaluation of an Organ-Targeted PET Camera	31
3.1.	Introduction	32
3.2.	Spatial Resolution	33
3.2.1.	Methods	33
3.2.2.	Results	34
3.3.	Sensitivity	35
3.3.1.	Methods	35
3.3.2.	Results	36
3.4.	Count Rate Performance	37
3.4.1.	Methods	37
3.4.2.	Results	38
3.5.	Micro Hotspot Phantom	40
3.5.1.	Methods	40
3.5.2.	Results	40
3.6.	Summary	41
4.	Clinical Performance Demonstration of Organ-Targeted PET Camera	42
4.1.	Introduction	43
4.2.	Methods	43
4.3.	Results	44
4.4.	Summary	48
5.	Evaluation of Quantitative Imaging Capabilities of a Clinical Organ-Targeted PET Camera	49
5.1.	Abstract	50
5.2.	Introduction	50
5.3.	Materials and Methods	54
5.3.1.	Spatial Resolution and Linearity	54
5.3.2.	Flood Field Uniformity	56
5.3.3.	Recovery Coefficients	56
5.3.4.	Image Quality Phantom	58
5.3.5.	Clinical Imaging Demonstration	61

5.4.	Results	61
5.4.1.	Spatial Resolution and Linearity	61
5.4.2.	Flood Field Uniformity	61
5.4.3.	Recovery Coefficients	62
5.4.4.	Image Quality Phantom	63
5.4.5.	Clinical Imaging	65
5.5.	Discussion	68
5.5.1.	Spatial Resolution & Linearity	69
5.5.2.	Image Uniformity	70
5.5.3.	Recovery Coefficients	70
5.5.4.	Image Quality Phantom	71
5.5.5.	Clinical Images	72
5.6.	Conclusion	74
6.	Thesis Summary and Conclusions	76
6.1.	Concluding Remarks	76
7.	References	78

## Table of Figures

Figure 1. A 1-dimensional schematic showing different possible PET coincidence events with a planar detector geometry.....	9
Figure 2. Expanded view showing components of the detector module designed for clinical organ-targeted PET. ....	16
Figure 3. 1-dimensional schematic showing the parallax effect in PET coincidence detection where LOR error occurs due to photon absorption within pixels adjacent to that upon which it impinged. Pixel coordinates are assigned to the surface of the crystal, regardless of the depth of interaction. ....	18
Figure 4. Left: 1-dimensional schematic presentation of the cross-section of three tiled detector blocks; Right: The photo of a block detector with crystal array wrapped in a light reflective material, tapered light guide and SiPMs array with an electronic board underneath. ....	19
Figure 5. A 1-dimensional schematic showing scintillation light-sharing over multiple SiPM pixels using a monolithic light guide in response to gamma photon detection. ....	20
Figure 6. Configuration of the Radialis organ-targeted PET Camera with two planar detector heads for positioning around an organ of interest.....	21
Figure 7. Detector schematic showing the overall size of the detector heads with 3x4 array of sensor modules per detector head and the axis convention for measurements.....	22
Figure 8. Block detector channel assignments with corresponding ADC for the purpose of decoding event coordinates for upper and lower detector heads A and B.....	26
Figure 9. Reconstructed system spatial resolution of a Na-22 point source measured per NEMA protocols with a MLEM reconstruction algorithm. Left: The central Z Axis resolution plotted as a function of point source location along the X Axis. Right: Quarter Z Axis resolution plotted as a function of point source location along the X Axis.....	35
Figure 10. Axial absolute sensitivity plotted against point source location along the X axis for the Radialis PET and Naviscan PEM Flex Solo II scanner <sup>44</sup> . ....	37
Figure 11. System count rate curves for low and full activity concentrations.....	39
Figure 12. Image of the micro hotspot phantom reconstructed using MLEM reconstruction algorithm. ....	41
Figure 13. A 56-year-old female with invasive ductal carcinoma and intermediate-grade DCIS. Digital mammography of right breast (A) and right breast Radialis PET image with 37 MBq	

18F-FDG injection (B) both in the same projection (CC view) are presented for comparison between these two imaging modalities. Cancers are demonstrated by the arrows (A, B) and arrowhead (B). The second cancer (arrowhead) is visualized only by Radialis PET (B). ... 44

Figure 14. A 61-year-old female with right breast multifocal invasive and in situ ductal carcinoma. Images of the same breasts in: A) FFDM in the CC plane showing extensive distortion; B) a selected slice of MRI in the axial plane showing one irregular shape enhancing mass lesion after 2 min post gadolinium-chelates based contrast administration; C) 3D Radialis PET in the CC plane where multiple distinct regions of contrast uptake after 1 hour of 178 MBq 18F-FDG injection are evident; (D) 3D Radialis PET in the CC plane where the conspicuity of the multiple regions of enhanced 18F-FDG uptake (indicative of multifocal cancers) remains after 3 hours from the prior (C) acquisition; (E) invasive carcinoma in the center of the field with in situ carcinoma present at the periphery in pathology of mastectomy specimen; (F) higher power view demonstrating intermediate grade invasive carcinoma on the right and papillary ductal carcinoma in situ on the left.... 45

Figure 15. The MLO view digital mammography image (A) demonstrated the palpable mass (red circle) associated with the radiopaque marker placed on the patient's skin. The presented slice of Radialis PET camera CC image with 200 MBq injected 18F-FDG (B) identifies this lesion against the chest wall as well as two additional posterior masses; (C) view of largest focus showing invasive ductal carcinoma no special type, clip site reaction is present in the center of the tumor; (D) second invasive focus demonstrating similar morphologic features and histologic grade. The 3 regions of contrast enhancement identified by Radialis PET were all biopsy confirmed cancers..... 46

Figure 16. A 33 years-old high-risk female underwent pre-operative breast MRI with multiplicity of enhancing masses demonstrated by the 3D-MIP image (A) and without corresponding masses demonstrated by the Radialis PET camera images (B) with a 43 MBq injection. The mediolateral oblique views from the Radialis PET camera are presented for the left (B) and right (C) side without evident focal 18F-FDG uptake in either image. The surgical pathology results do not show signs of cancer..... 47

Figure 17. Side by side comparison of 307 MBq PET images from a breast cancer patient scanned with a Siemens Biograph PET/CT reconstructed using a time-of-flight reconstruction technique (TOF) (A and B) and with the Radialis PET system (C). ..... 48

Figure 18. Schematic diagram of the fillable capillary phantom (top) and spatial linearity phantom (bottom) with markings for the line source separation and phantom dimensions. 55

Figure 19. Schematic diagram of the acquisition layout for the recovery coefficient experiment showing hot spheres of radioactivity positioned between two IV bags for background activity and immobilized between detector heads. Note that the schematic is not to scale.. 57

Figure 20. Design configuration and dimensions in mm of the NEMA NU-4 Image quality phantom. Source: [www.qrm.de/en/products/micro-pet-iq-phantom](http://www.qrm.de/en/products/micro-pet-iq-phantom) ..... 59

Figure 21. Reconstructed images showing the hot spheres and IV bags at sphere to background activity concentrations of 4:1 (A) and 10:1 (B). Note that visual non-uniformity in central regions of the bags is a result of the plastic hot-sphere fixture and a gap in activity at the physical interface between bags..... 62

Figure 22. Reconstructed image slices for the NEMA NU-4 image quality phantom displaying the hot rods with diameters 1 - 5 mm for recovery coefficients (A), uniform region (B), and the air and water reservoirs (C)..... 64

Figure 23. Images acquired for a 61-year-old female with right breast multifocal invasive and in situ ductal carcinoma. Images show the same breast in: A) FFDM in the CC plane with extensive distortion; B) 3-D Radialis PET image in the CC plane 1 hour after 178 MBq 18F-FDG injection; C) 3-D Radialis PET image in the CC plane where multiple distinct regions of contrast uptake are still evident 4 hours after 18F-FDG injection. Mean lesion SUV corrected for lean body mass (SUV<sub>mean</sub>, LBM) is 1.8, with SUV<sub>max</sub>, LBM equal to 3.4.; (D) image of a 3-D volume of different foci generated from Radialis PET in the CC view based upon percentage of SUV<sub>max</sub> tissue metabolism across all image slices..... 66

Figure 24. A 56-year-old female with invasive ductal carcinoma and intermediate-grade DCIS underwent FFDM imaging (A) with red arrow indicating the site of a primary lesion. Radialis PET image (B) acquired 1-hr after injection with 37 MBq 18F-FDG and same craniocaudal (CC) view shows two distinct sites of contrast enhancement. The second site (arrowhead) is not detected in mammography. Both sites were confirmed cancerous by histopathology. 3-D volume (C) generated from the Radialis PET in the CC view based upon tissue metabolism threshold across all image slices. SUV<sub>mean</sub>, LBM for the primary lesion is 5.3, with SUV<sub>max</sub>, LBM equal to 12.2. SUV<sub>mean</sub>, LBM for the secondary lesion is 5.3, with SUV<sub>max</sub>, LBM equal to 10.7. .... 67

Figure 25. Clinical images acquired for two female patients with invasive lobular carcinoma who underwent x-ray mammography (A & B) and Radialis PET imaging 4-hours after radiotracer injection. The 50-year-old patient (A & C) received 188 MBq 18F-FDG injection and the image shows CC view mammography and PET images. SUV<sub>mean</sub>, LBM for the lesion in (C) is 6.8, with SUV<sub>max</sub>, LBM equal to 14.9. The 58-year-old patient (B & D) received 191 MBq 18F-FDG injection and the image shows a mammographic and Radialis PET mediolateral oblique (MLO) view. SUV<sub>mean</sub>, LBM for the lesion in (D) is 2.2, with SUV<sub>max</sub>, LBM equal to 4.4. Surgical pathology confirmed both lesions visible in the PET images as invasive lobular carcinoma..... 68

**Table 1.** Summary of common PET tracer radioisotopes and their means of production. [,]..... 4

**Table 2.** Summarized linear attenuation coefficients for different materials relevant to PET imaging at 511 keV photon energy. .... 8

**Table 3.** Summary of performance metrics for selected scintillator materials. [,]..... 16

**Table 4.** Summarized performance parameters for SensL ArrayC SiPM sensors at operational bias voltage. .... 19

**Table 5.** Summary of ADC module specifications for the Radialis PET Camera ..... 24

**Table 6.** Summary of trigger module specifications for the Radialis PET Camera. .... 24

**Table 7.** Summary of measured FWHM and FWTM spatial resolution in for a detector head separation of 80mm using MLEM reconstruction. .... 35

**Table 8.** Summarized values for count rates at different LOR angle allowance parameters. .... 39

**Table 9.** Summary of pixel value uniformity results for the 1st and 15th iterations..... 62

**Table 10.** Summarized recovery coefficients and percent contrast for Radialis PET and two other commercial organ-dedicated PET scanners from phantom experiments. Quoted spatial resolution values are provided for comparison. [44,46,66 ,68] ..... 63

**Table 11.** Contrast to Noise ratio for each sphere size and sphere to background activity concentrations with corresponding Rose Criterion assessment. .... 63

**Table 12.** Summarized recovery coefficients, spill-over ratio and percent standard deviation for NEMA NU-4 phantom hot rods and cold cylinders for Radialis PET and another commercial organ-dedicated PET scanner [66,68]..... 65

<b>Table 13.</b> Lean body mass corrected standardized uptake values for breast lesions in Figures 21-23.....	73
---	----

## List of Acronyms

PET	Positron Emission Tomography
WB	Whole Body
$^{18}\text{F}$ -FDG	2-deoxy-2-[fluorine-18] fluoro-D-glucose
CT	Computed Tomography
MRI	Magnetic Resonance Imaging
SPECT	Single-Photon Emission Computed Tomography
Bq	Becquerel (SI Unit)
Ci	Curie (SI Unit)
eV	Electron Volt
MeV	Mega Electron Volt
PE	Photoelectric Effect
LOR	Line Of Response
FWHM	Full Width at Half Maximum
FWTM	Full Width at Tenth Maximum
PMT	Photomultiplier Tube
FOV	Field Of View
PD	Photodiode
APD	Avalanche Photodiode
SiPM	Silicon Photomultiplier
DCR	Dark Count Rate
NECR	Noise Equivalent Count Rate
LYSO	Lutetium Yttrium Oxyorthosilicate
BGO	Bismuth Germanate
CSI	Cesium Iodide
IO	Input Output
CC	Craniocaudal
MLO	Mediolateral Oblique
PCB	Printed Circuit Board
DAQ	Data Acquisition
ADC	Analog to Digital Converter

LVDS	Low Voltage Differential Signaling
UDP	User Datagram Protocol
EMI	Electromagnetic Interference
DMP	Dump File
DICOM	Digital Imaging and Communications in Medicine
MLEM	Maximum Likelihood Expectation Maximization
MRP	Median Root Prior
OSEM	Ordered Subsets Expectation Maximization
MAP	Maximum A Posteriori
ETM	Estimation of Trues Method
NEMA	National Electrical Manufacturers Association
PEM	Positron Emission Mammography
PSF	Point Spread Function
SSRB	Single Slice Re-Binning
SUV	Standardized Uptake Value
SNR	Signal to Noise Ratio
UHN-PMCC	Princess Margaret Cancer Centre of the University Health Network
FFDM	Full Field Digital Mammography
DCIS	Ductal Carcinoma In Situ
TOF	Time of Flight
NST	Neoadjuvant Systemic Treatment
PVE	Partial Volume Effect
RC	Recovery Coefficient
CNR	Contrast to Noise Ratio
LSF	Line Spread Function
STD	Standard Deviation
ROI	Region of Interest
LBR	Lesion to Background Ratio
SOR	Spill Over Ratio
VOI	Volume of Interest
ILC	Invasive Lobular Carcinoma

LBM	Lean Body Mass
IDC	Invasive Ductal Carcinoma

## 1. Introduction

### 1.1. Principles of PET Imaging

Positron emission tomography (PET) is a molecular imaging modality. When applied with specific radiopharmaceuticals, it permits visualization and quantitative in vivo assessment of physiological and biological phenomena in the human body which may be critical in management of various diseases. A PET radiopharmaceutical (or radiotracer) consists of a positron-emitting isotope bound to an organic ligand. The ligand is selected to target a specific physiological or pathological function in the body, such as glucose metabolism, protein synthesis, receptor binding, etc. [1] The radiotracer is administered to the patient intravenously and subsequently undergoes rapid distribution throughout the body, accumulating in target tissues or process.

The positron-emitting radionuclide decays via positron ( $\beta^+$ ) emission. The emitted positron typically has a high kinetic energy and thermalizes through electrostatic interactions with the electrons and atomic nuclei of the surrounding tissue. This process determines the positron range, which can vary from sub-millimeters to a few millimeters, depending on the initial kinetic energy of the positron.

Once the positron has lost its kinetic energy, it undergoes annihilation with an electron in the surrounding matter, producing two photons with an energy of 511 keV, which are emitted in opposite directions. Some fractional kinetic energy still exists upon annihilation, resulting in noncollinearity which is discussed in 1.2.5. PET detectors capture these time-correlated photon pairs and reconstruct the location of the annihilation events, enabling the visualization of the radiotracer distribution and its increased uptake in targeted tissues. PET scanners can be configured either as WB PET systems, where a ring of detectors surrounds the patient, or as organ-targeted systems, where planar or ring detectors are placed around an organ of interest. Regardless of the configuration used, PET imaging provides information about the location and concentration of the radiotracer, which reflects the underlying physiological or pathological process being targeted.

The most frequent application of PET is in oncology, where measurement of 2-deoxy-2-[fluorine-18] fluoro-D-glucose ( $^{18}\text{F}$ -FDG) radiotracer, a glucose analogue, can indicate cells exhibiting an abnormally increased glucose metabolism - an important cancer biomarker, and

may depict metabolic abnormalities before morphological alterations become detectable. PET is particularly useful in situations where conventional imaging modalities such as X-ray, Computed Tomography (CT), or Magnetic Resonance Imaging (MRI) are limited in their ability to differentiate normal from abnormal tissues or provide information about molecular function. PET also offers distinct advantages in cancer detection when compared with other nuclear medicine tomographic imaging, namely single-photon emission computed tomography (SPECT). Detection of two annihilation photons in coincidence offers the fundamental advantage since this eliminates the need for a collimator (an inherent component of SPECT systems) and yields improved spatial resolution, detection sensitivity, and the ability to quantify tracer uptake in tissues [2].

Advancing technologies have increased the capabilities of clinical PET scanners and created new possibilities for clinical use, including cancer detection and staging, monitoring response to cancer therapy through lesion metabolic assessment and post-surgical follow-up. With the development of new radiotracers and imaging technologies, it is likely that PET will continue to play a prominent role in clinical practice, including applications beyond cancer and in biomedical research.

### 1.1.1. Radioactive Decay and Positron Emission

Radioactive decay is a phenomenon which refers to the spontaneous transformation of an unstable and energetically imbalanced nucleus to a more stable configuration through the emission of particles or electromagnetic radiation. The rate of radioactive decay is described mathematically by an exponential function, where the rate of decay is proportional to the number of pre-decay atomic nuclei present. The rate of decay is commonly referred to as *activity* and is dependent on the half-life of the isotope, or time elapsed over which half of observed nuclei will decay. The remaining activity after some elapsed time,  $A(t)$ , is proportional to the initial activity  $A(0)$  and depends on the half-life  $\tau$ , which is captured within the exponential term of the function:

$$A(t) = A(0)e^{-t\left(\frac{\ln 2}{\tau}\right)} \quad \text{Equation 1}$$

The activity of a radioisotope is measured in the SI unit Becquerel (Bq), with 1 Bq equal to 1 decay per second. An alternative reference is the traditional unit of Curie (Ci), with 1 Ci equal to  $3.7 \times 10^{10}$  Bq.

Radioactive decay by positron emission occurs due to a destabilizing balance of neutrons and protons in the nucleus. When the number of protons in the nucleus is greater than the number of neutrons so that the nucleus is no longer stable, a transition occurs from a proton ( $p^+$ ) into a neutron ( $n$ ) and positively charged positron ( $\beta^+$ ), the antiparticle of a negatively charged electron ( $\beta^-$ ). The process is described as follows:



where  $p$  is a proton,  $n$  is a neutron,  $\beta$  is a positron, and  $\nu$  is a neutrino. The process is

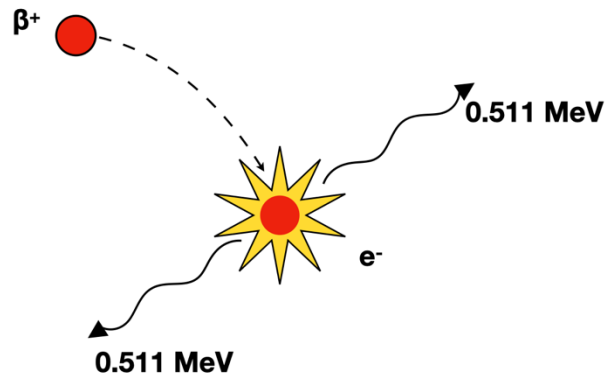


Figure 1. Schematic representation of mutual-annihilation between interacting positron ( $\beta^+$ ) and electron ( $e^-$ ). A pair of antiparallel 0.511 MeV photons are emitted from the interaction.

followed by positron - electron annihilation, resulting in the emission of two gamma rays in opposite directions (Figure 1). Electron capture is an alternative mechanism by which the unstable nucleus with an abundance of protons absorbs a K or L shell electron to convert a proton into a neutron to stabilize with emission of an electron neutrino.

### 1.1.1. Positron Range and Annihilation

The straight-line distance from the origin nucleus to the site of annihilation is referred to as the positron range and depends on factors such as initial positron kinetic energy and interaction cross-section of surrounding matter (in other words, the properties of the tissue within which it is traveling). The positron range is a critical factor in PET imaging since it affects the PET detector's ability to accurately determine the location of the positron emission event and imposes a fundamental limit on spatial resolution. When

the positron range is comparatively long (in the range of mm), the detected annihilation event may occur some distance away from the actual site of positron emission. This results in PET image blur and a loss of spatial resolution. Thus, the positron kinetic energy and range must be considered when determining radiotracer applicability for a particular clinical application. Radiotracers with less positron kinetic energy and shorter positron ranges are more suitable for pre-clinical and organ-targeted clinical PET imaging, where high spatial resolution is required to allow detectability of small structures, such as small tumors.

The maximum positron kinetic energies and corresponding half-lives are reported for several common PET radionuclides in Table 1.  $^{18}\text{F}$  is the most common isotope used for cancer detection in breast and is chemically bound to glucose molecules for clinical use as  $^{18}\text{F}$ -FDG.

Table 1. Summary of common PET tracer radioisotopes and their means of production. [3,4]

Radionuclide	Half-Life	$\beta^+$ range in water (mm, mean)	$\beta^+$ energy (MeV, max)	Production
C-11	20.4 min	1.2	0.960	Cyclotron
N-13	9.96 min	1.8	1.19	Cyclotron
O-15	123 sec	3.0	1.72	Cyclotron
F-18	109.8 min	0.6	0.635	Cyclotron
Cu-64	12.7 hours	0.7	0.653	Cyclotron
Ga-68	68.3 min	3.5	1.9	Ge-68 Generator
I-124	4.18 days	2.3	1.5	Cyclotron

## 1.2. Photon Detection

### 1.1.2. 511 keV Photon Interactions in Matter

Annihilation gamma photons can pass through the body without interacting due to their high energy, which is much greater than the binding energies of the electrons in surrounding tissue. This permits the gamma photons to escape the body unattenuated and to be detected as true coincident events, which is crucial in accurately reconstructing an image of the radiotracer distribution within the body.

However, the quantity of tissue which the photons must traverse before detection by PET sensors requires that some fraction of annihilation gamma photons cannot avoid

interaction and will still be attenuated in the body through absorption (complete energy deposition in matter) or scattering (change in direction, with or without loss of energy). The interaction probability depends on the energy of the photon and the density of the surrounding tissue, such as soft tissue or bone. The two primary mechanisms of 511 keV photon interactions in matter, including patient tissues or detector materials, are the photoelectric interaction and Compton scattering.

### **1.2.1. Photoelectric Interaction**

The photoelectric interaction is a fundamental mechanism of gamma photon interaction with matter. In this process, a photon interacts with an atom in the material, and all its energy is transferred to an inner-shell electron, typically a K or L-shell electron. The probability of this interaction increases with the atomic number of the material and decreases with the photon energy. In PET imaging, the energy of the annihilation photon (511 keV) is typically much greater than the binding energy of the electron in any tissue or detector material, ensuring the prerequisites for the photoelectric effect are satisfied.

Once the photoelectric interaction occurs, the atom is left in an excited state with a vacancy in the K or L-shell. The atom quickly relaxes to its ground state by emitting characteristic X-rays or Auger electrons, which deposit their energy locally and are typically absorbed within a few millimeters from the interaction site. The photoelectric effect (PE) is the dominant interaction for 511 keV gamma photons with dense (high  $Z$ ) materials such as PET detectors. Photons emanating directly from the site of annihilation in the patient's body may interact and deposit their energy in the detector via PE and result in a photopeak in the measured energy spectrum.

### **1.2.2. Compton Scattering**

Compton scattering is another important mechanism of gamma photon interaction with matter, which occurs when a photon collides with an outer-shell electron in an atom. In this process, the incident photon undergoes a reduction in energy and changes its direction, while the scattered electron is ejected from the atom with a fraction of the photon's energy.

The change in direction from the photon's original path is governed by conservation of momentum and energy, from which a mathematical relation is derived between the

incident photon energy ( $E_i$ ), scattered photon energy ( $E_s$ ), and the angle by which the photon is scattered ( $\theta$ ):

Equation 3

$$E_s = \frac{m_e c^2}{\frac{m_e c^2}{E_i} + 1 - \cos \theta}$$

The equation describes scattered photon energy, where  $m_e$  is the electron mass,  $c$  is the speed of light ( $2.998 \times 10^8$  m/s). The numerator ( $m_e c^2$ ) is equal to 511 keV when units of electron volts are used for energy, and since the photons in question for PET imaging are emitted at 511 keV, the equation for scattered photon energy in units keV is simplified:

Equation 4

$$E_s = \frac{511}{2 - \cos \theta}$$

The energy which is imparted to the electron ( $E_e$ ) by the incident photon ( $E_i$ ) and is absorbed in the medium is described by:

Equation 5

$$E_e = E_i - E_s = E_i \times \frac{1 - \cos \theta}{\frac{m_e c^2}{E_i} + 1 - \cos \theta}$$

Making the prior substitution for photon energy equal to 511 keV, we have:

Equation 6

$$E_e = 511 \times \frac{1 - \cos \theta}{2 - \cos \theta}$$

As seen from Equation 5 and Equation 6, the amount of energy transferred to the electron and the surrounding matter by the incident photon depends on the angle at which the photon is scattered. When the scattered angle is  $180^\circ$ , the energy transfer is at its maximum and produces a Compton edge in energy spectra to the left of the photopeak.

Compton scattering is a major source of blur and noise in PET imaging, which can affect the accuracy of diagnostic images. Partial energy deposition in the detectors due to Compton scattering can lead to uncertainties in the detection process since the scattered photons can be detected as if they were directly emitted by the radiotracer, leading to scatter coincidence events. While Compton scatter events are conceptually true coincidences, the LOR formed from these events is less precise than LORs formed from events involving photoelectric absorption due to the deflection of scattered photons before they are detected.

Moreover, the scattered photon can travel a considerable distance before undergoing further interactions or being detected, thus reducing the spatial resolution of the PET system. The probability of Compton scattering depends on the energy of the photon and the atomic number of the material. At the photon energies used in PET imaging (511 keV), the probability of Compton scattering is relatively high in low-density materials, such as soft tissues in a patient's body or plastic parts of PET detectors and decreases as the density of the material increases.

To minimize the impact of Compton scattering, PET detectors are designed with a high-density material to increase the probability of photon absorption and reduce the distance traveled by the scattered photons. Additionally, mathematical algorithms are employed to distinguish true coincidence events from those caused by Compton scattering, thus improving image contrast. A PET scatter correction algorithm is described further in 2.5.4.

### **1.2.3. Interaction Cross-Section in Matter**

The probability of absorption or scattering photon interactions in different materials relevant to 511 keV photons is described by:

Equation 7

$$I(x) = I(0)e^{-\mu x}$$

Here,  $I(x)$  is the output flux which passes through the medium without interaction,  $I(0)$  represents the 511 keV photon flux which is incident on the medium,  $x$  is the thickness of the sample, and  $\mu$  is the linear attenuation coefficient for the medium describing interaction probability per unit distance. The attenuation coefficient for 511 keV photons in matter is predominantly comprised of Compton scattering and photoelectric absorption interactions and thus  $\mu$  is the collective sum of their respective attenuation coefficients.

Attenuating matter may be classified into several categories in the context of PET imaging: biological tissues, detector materials, and shielding materials. Biological tissues consist of those which comprise the patient, namely soft tissues (muscle, fat, fluids) and bone. Properties of the various tissues influence photon interaction probabilities and influence the ability to accurately reconstruct the true origin of detected photons. Unlike biological tissues, the detector material is specifically selected to be highly attenuating for 511 keV photons while also providing a scintillation light output in response to photon

absorption which can be measured with a photosensor. Finally, shielding materials are selected to be highly attenuating to the 511 keV photons to protect sensitive materials and to shield persons other than the patient from unwanted exposure. Summarized attenuation coefficients and the material thickness to attenuate 50% incident photon flux are given in Table 2.

Table 2. Summarized linear attenuation coefficients for different materials relevant to PET imaging at 511 keV photon energy.

Material	$\mu_{Compton} (cm^{-1})$	$\mu_{photoelectric} (cm^{-1})$	$\mu (cm^{-1})$	Half-value thickness (cm)
Soft tissue	~0.096	~0.00002	~0.096	7.2
Bone	~0.169	~0.001	~0.17	4.1
Lead	0.76	0.89	1.78	0.42
Tungsten	1.31	1.09	2.59	0.29

It is apparent that the photon interaction cross section is significantly lower in biological tissue, particularly soft tissue, and that the dominant interaction is Compton scatter. As a result, we expect that a certain portion of photons recorded by the PET detectors will have undergone some degree of angular scatter from their original trajectory before falling incident on the detector surface. Scattered annihilation photons can result in random detection correlations and incorrect location assignments during image reconstruction. From our understanding of energy transfer in Compton scattering, we can infer to what extent a detected photon may have been diverted from its straight-line trajectory by accurately measuring its energy upon detection.

#### 1.2.4. Detection of annihilation radiation in PET imaging

Detection of time-correlated annihilation photon pairs requires at least a pair of opposite detectors (or a ring detector) that are optimized for detection of high energy photons of 511 keV. A typical PET detector comprises of a scintillation crystal (used to convert gamma-photons into a visible or ultraviolet light) optically coupled to an array of photosensors. Photosensors convert scintillation light into measurable signal which is further processed by readout electronics and data acquisition system to estimate the energy and registration coordinate of the coincidence gamma photon and reconstruct a LOR along which annihilation event occurs.

Different PET coincidence events are illustrated in Figure 1. A coincidence event where photons are detected from the same annihilation and without subsequent interaction in the body is termed a “true coincidence” event. A “random coincidence” is an event which occurs when only one 511 keV photon from a positron annihilation is detected, the other being attenuated or missing the opposing detector, and an unrelated 511 keV photon is detected within the coincidence timing window. This random coincidence is a source of error which results in a false set of coordinates assigned to a positron annihilation.

Additional sources of error occur when one or both annihilation photons are scattered from their original trajectory yet still detected within coincidence timing. This “scatter coincidence” results in a LOR which does not correspond to the site of annihilation despite detection of both annihilation photons and produces blur in the reconstructed image. Finally, “attenuation error” occurs as a result of one or both annihilation photons being absorbed in tissue or scattered from the FOV prior to detection, resulting in no coincidence detection for the annihilation event and reduced total counts for reconstruction. Several corrective steps may be applied within the image reconstruction workflow to ensure accuracy and integrity of reconstructed images by selecting for true coincidence

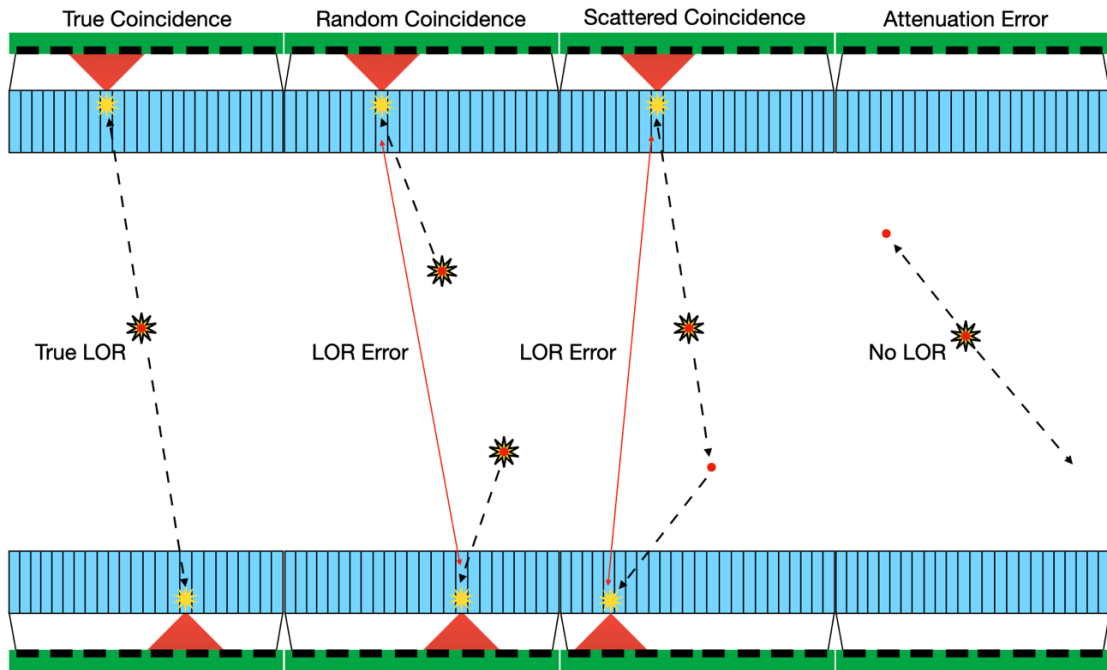


Figure 1. A 1-dimensional schematic showing different possible PET coincidence events with a planar detector geometry.

data and minimizing the effect of scattered photons on the true signal. These corrective

steps include attenuation and scatter corrections, as well as photon energy and angular filtration, all of which shall be described in a subsequent section.

### **1.2.5. Noncollinearity**

An important consideration for data integrity in PET is that positrons which annihilate are not completely at rest, and therefore some non-zero momentum is present. To conserve momentum, the annihilation photons are emitted at angles which differ from the ideal 180° and this effect is referred to as noncollinearity. The result of this effect is error in the LOR assigned to the detected annihilation photons since the reconstruction algorithm assumes the ideal 180° antiparallel photon emission.

The magnitude of noncollinearity may be estimated using trigonometry due to the small angles of misalignment and described by:

Equation 8

$$\Delta_{noncollinearity} = 0.0022D$$

Here,  $D$  represents the diameter of PET ring detector and serves as an approximation for distance between detectors in the planar geometry described here. It should be noted that there is a linear increase in error due to noncollinearity with increased detector separation, and that the error is not dependent on initial positron kinetic energy. Since detector separation in organ-targeted PET systems is smaller than in WB PET, the effect of non-collinearity on resolution is lesser.

### **1.3. Scintillation Material**

The scintillation process in practical PET detectors is a two-step process. First, the incident gamma photon deposits energy in the scintillator material, causing electrons to transition to excited metastable energy states. The second step is the de-excitation process, during which the excited electrons decay back to their stable ground states and release energy in the form of light. This light emission is referred to as scintillation light and is proportional to the amount of energy deposited by the gamma photon. The detection of this scintillation light by photodetectors allows for the localization and quantification of gamma photons emitted from the radiotracer, enabling the creation of an image of radiotracer distribution.

The scintillator material is specifically selected for properties suited to PET imaging. These properties include the material's photon stopping power, energy resolution, light output, and

decay constant. Stopping power is defined as a photon's inverse mean distance travelled before energy deposition in the scintillation material. A short distance indicative of high stopping power is desirable, as it will result in more 511 keV photon interactions and therefore a more complete deposition of its energy in a material of finite thickness. The distance travelled by a photon in the material is dependent on material density and effective atomic number  $Z$ .

Energy resolution describes the ability to accurately identify the energy of interacting photons. Desirable energy resolution is a result of low variance in measured energy for equivalent photons and depends on the scintillation light output and the material's intrinsic energy resolution. This provides the ability to differentiate between photons which have lost energy due to Compton scattering and can be selectively filtered to reduce inaccuracies during image reconstruction. Energy resolution is often quoted as the full width at half maximum (FWHM) of a peak on a measured energy spectrum, normalized for the known photon energy.

A scintillation material's light output describes the quantity of photons emitted in response to absorption of each incident 511 keV photon. A highest-possible light output is generally desired for greatest intrinsic signal gain. This signal gain allows for improvements in spatial and energy resolution of the detector. The time over which this light output occurs is described by the material's decay constant. A short-as-possible decay constant (in the range of  $\mu\text{s}$ ) allows for higher count rate capabilities by minimizing detection deadtime. The most common scintillation crystals for PET are summarized in Table 3.

#### **1.4. Photosensors**

The most common photosensors used in PET imaging are vacuum photomultiplier tubes (PMTs). PMTs have a cathode that is sensitive to photons and converts them into electrons through photoelectric interactions. These electrons are then accelerated using a high applied bias voltage and pass through multiple dynode stages, which amplifies the electron signal by secondary emission of additional electrons. This process results in high signal gain of about  $10^6$  electrons for each incident photon [5], and the arrival of these electrons at the anode produces a current pulse that is proportional to the number of incident photons. The photons are proportional to the energy deposited by the 511 keV photon in the scintillation material, and the anode current provides a measure of the original photon energy.

The use of PMTs in PET detectors has advantages such as high gain and low noise. However, it also has some disadvantages, including linearity distortion in the image, dead

space between the Field-of-View (FOV) and the physical edge of the detector, bulky detector system due to PMT size, and inadequate spatial resolution for detecting small lesions. PMTs have a low quantum efficiency ( $\sim 25\%$ ) [6], which can cause degradation of energy resolution, especially for scintillators with poor light output. High spatial resolution requires much higher segmentation of scintillators than what is typically used in PMT-based PET cameras, as well as the ability to readout each segment independently [7]. PMTs are also fundamentally sensitive to magnetic fields, which precludes their use in combined PET/MRI applications.

Silicon-based solid-state photodetectors offer a potential solution to the drawbacks of PMT-based sensors. These detectors include photodiodes (PD), avalanche photodiodes (APD), and APDs operating in Geiger mode. Compared to PMTs, silicon-based detectors are thin and less bulky, making them suitable for compact read-out devices produced in arrays. Both PDs and APDs have higher quantum efficiency (40-65%) [8] and better lateral uniformity than PMTs. However, PDs provide no gain and thus require a charge-sensitive amplifier per channel, which adds cost and noise to the readout system [6]. Inadequate energy resolution, timing resolution, and signal-to-noise ratio are also issues with PDs.

APDs have an advantage over PDs as they have internal gain, although this is not always adequate [9], and the gain is temperature dependent, making the energy window sensitive to small temperature changes. SiPMs, also known as silicon photomultipliers, offer a further increase in gain by using Geiger breakdown mode, making them the semiconductor equivalent of vacuum PMTs with a single-photon sensitivity for UV to visible light. This ushered a new era in solid-state PET technology [10]. SiPMs also benefit from practical advantages of solid-state technologies, including a low operating voltage, temperature stability, robustness, compactness, output uniformity, and relatively low cost. [11] In addition, SiPMs are inherently insensitive to magnetic field that is of a paramount importance for dual-modality PET/MRI scanners.

Conceptually, a SiPM is a 2-D matrix of silicon avalanche photodiodes (APDs) microcells (or pixels), each operated in Geiger-mode, joined on a common substrate with a common quenching resistor. The typical pixel size for SiPMs ranges from a few tens of micrometers to a few hundred micrometers, and the number of APDs in a SiPM can range from a few hundred to several thousand, depending on the size of the device, the manufacturer, and the required dynamic range.

Each APD contains a p-n junction that is reverse-biased by applying a positive voltage to the n-type region and a negative voltage to the p-type region. The reverse bias creates a depletion region, which is widened by an intrinsic (i) region between the p and n doped layers (forming a p-i-n junction), to increase the probability of photon absorption. When an optical photon is absorbed in the depletion region, it generates an electron-hole pair. The electric field in the depletion region accelerates these charges towards the opposite electrodes, producing a photocurrent. However, if the reverse bias voltage is increased beyond a certain threshold, called the breakdown voltage ( $V_{Br}$ ), it triggers impact ionization and avalanche formation, resulting in significant multiplication of the initial photocurrent. The quenching resistor defines the maximum photocurrent and hence the multiplication gain.

The parallel connection of individual APDs in a SiPM makes a linear device with the dynamic range given by the number of microcells: when multiple APDs are triggered by scintillation light photons, the output signal is proportional to the quantity of the fired APDs (or, incident light photons) and therefore the energy of the gamma photon that is absorbed in a coupled scintillator. The use of a common quenching resistor ensures that each APD returns to its unbiased state after each avalanche event, allowing the device to operate in a stable and reliable manner.

Intrinsic amplification in silicon photodiodes also results in amplified noise called dark current. At the current stage of SiPM technology, the major source of dark current is the charges generated within the depletion region due to thermal generation or band-to-band tunnelling. Thermally generated or tunneled electrons may trigger spontaneous Geiger breakdown in a microcell which will release the same charge as when a photon is detected. These dark signals are termed "Dark Counts" and are indistinguishable from actual photon counts. The frequency of these events is termed the "Dark Count Rate" (DCR) and the sum of all the dark counts generates the "Dark Current" of an SiPM. Two factors influence the DCR for a given SiPM, the overvoltage (that increase the breakdown probability and therefore the DCR) and the temperature (that increases the probability of thermal generation or band-to-band tunnelling). For this reason, temperature stabilization during SiPM operation is an important technical task.

The latest SiPM technology has continued to advance, with manufacturers offering devices with smaller pixel sizes, larger number of pixels and improved performance in terms

of the dynamic range and gain uniformity. One trend in SiPMs technology is the use of deeper junctions, which can improve the photon detection efficiency at peak emission from the scintillation crystals used in PET. The pairing of a high-light yield scintillation crystal with specially designed SiPMs with temperature stabilization is the basis for the high-resolution organ-targeted PET detector described herein.

## 2. Design of an Organ-Targeted PET Camera

### 2.1. Introduction

The ongoing emergence of new radiotracers for PET imaging is playing an increasingly important role in clinical practice. By allowing for the precise visualization and measurement of specific biological processes within the body, these tracers are helping to advance the field of personalized (or precision) medicine, which aims to tailor treatments to individual patients based on their unique characteristics and needs [12, 13, 14, 15]. In addition to scanning of the body with sequentially performed WB PET/CT scanners and emerging simultaneous PET/MRI, the applications for PET imaging increasingly involve the visualization of specific organs with dedicated systems [16, 17, 18, 19]. Compared to WB PET scanners, an organ-targeted PET system is capable of higher sensitivity, higher spatial resolution and higher signal-to-noise ratio resulting in better image contrast and enabling more precise PET examinations. Indeed, an organ-targeted PET camera with optimized geometry can position detectors in close proximity to the organ of interest to facilitate 1) more efficient gamma-ray detection; 2) higher spatial resolution; and 3) reduced unwanted signal from elsewhere in the body, improving the noise equivalent count rate (NECR) within the field of view due to a reduction of false coincidences [18, 19, 20, 21]. This may significantly lower a radiotracer dose thereby reducing radiation exposure associated with PET molecular imaging. The research in Reznik's lab has led to a new type of large-area high-resolution organ-targeted PET imager with improved sensitivity, capable of significant dose reduction (factor of 10) in comparison to both WB PET imagers and commercially available organ-targeted PET systems [66]. The improvement was made possible by maximizing 511 keV photon detection efficiency and spatial resolution with a new type of four-side tileable sensor modules based on SiPMs photosensors and Lutetium yttrium oxyorthosilicate (LYSO) scintillation crystals. Due to the patented four-side tileability, individual modules can be seamlessly combined – without gaps or dead zones – into a sensor area of a needed FOV as discussed below.

## 2.2. High-Performance PET Detector Technology

Figure 2 shows the detector module designed for the purpose of high-resolution organ-targeted PET. Each module consists of an SiPM photosensor array which is optically coupled through a tapered and polished borosilicate light-guide joining to an LYSO scintillation crystal array. Careful consideration of the fundamental physics has permitted the design and experimentation required to achieve the desired PET detector performance.

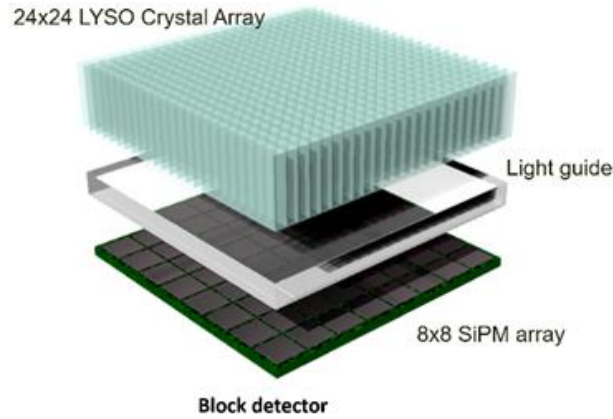


Figure 2. Expanded view showing components of the detector module designed for clinical organ-targeted PET.

A cerium-doped LYSO scintillation material was selected for the organ-targeted PET detector. LYSO has become a prominent inorganic scintillator in nuclear physics and is emerging in nuclear medicine. It is characterized by a set of qualities which render it particularly well-suited for applications in organ-targeted PET, including a high density and stopping power, short decay time, and high energy resolution (Table 3). The scintillation light emission spectrum peaks at 420 nm, which pairs very well with the spectral sensitivity of the SiPM. LYSO is also non-hygroscopic, thus not requiring hermetic sealing of detectors. As seen

Table 3. Summary of performance metrics for selected scintillator materials. [<sup>22</sup>, <sup>23</sup>, <sup>24</sup>]

Material	Density (g/cm <sup>3</sup> )	Decay time (ns)	Energy Resolution (at 662 keV)	Light output (photons/keV)
Lutetium yttrium oxyorthosilicate (LYSO)	7.1	45	7.1%	32
Bismuth germanate (BGO)	7.1	300	11.3%	10
Cesium iodide (CsI)	4.5	1000	6.0%	54

from Table 3, the use of LYSO crystal is advantageous compared to other scintillation crystals used in PET, namely BGO (Bismuth Germanate) and CsI (Cesium Iodide). One of the main performance indicators for PET scintillation crystals is light output: a higher light output in response to a given amount of energy deposition produces greater intrinsic energy resolution and detection sensitivity. Although light output and, as a result, energy resolution in LYSO is lower than in CsI, this is outweighed by the significantly shorter decay time in LYSO which means that it produces scintillation light with a shorter duration. This results in a higher rate capability, which is beneficial for applications that require high counting rates such as PET. It also has a higher density than CsI which means that it can be made thinner and thus reducing the parallax effect. The parallax effect is a source of error in PET and is produced by LORs which are not normal to the detector surface, as seen in Figure 3. When a photon enters a matrix of detector elements at an oblique angle, energy may be deposited at an unknown depth within the element which it entered, or the photon may exit to deposit energy in an adjacent element. These effects become increasingly problematic for detectors with large FOV, despite the improved detection sensitivity. Also, thinner scintillation crystals reduce detector size and weight, which is beneficial to make compact detectors. The scintillation crystal with the same density, i.e., BGO, has a lesser light output and longer decay time which may not be favorable for certain applications.

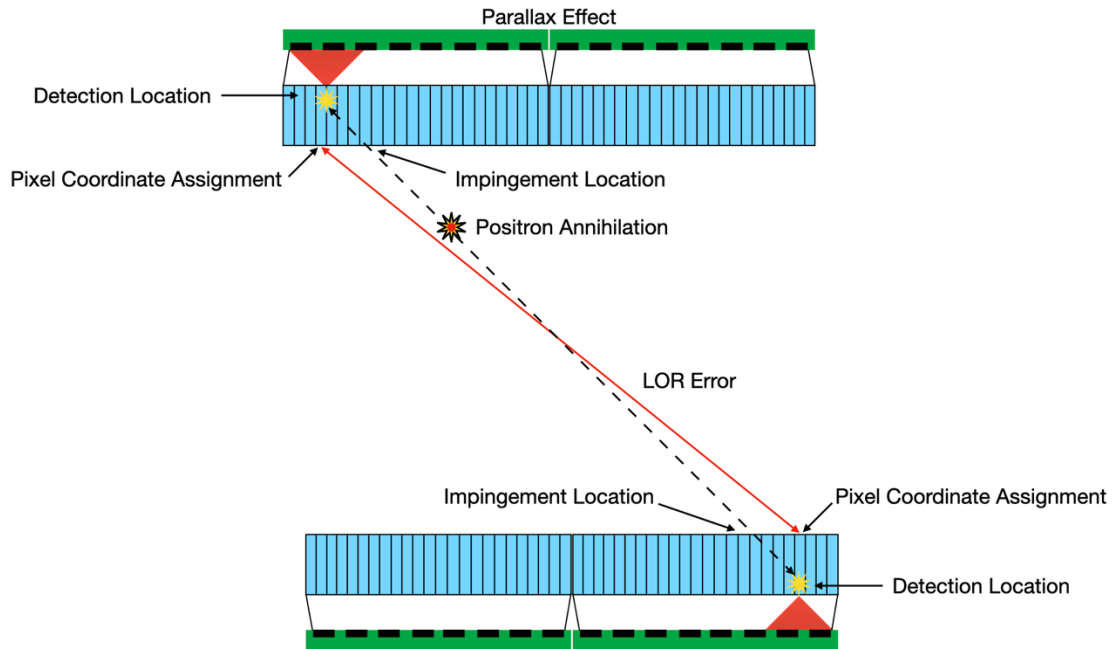


Figure 3. 1-dimensional schematic showing the parallax effect in PET coincidence detection where LOR error occurs due to photon absorption within pixels adjacent to that upon which it impinged. Pixel coordinates are assigned to the surface of the crystal, regardless of the depth of interaction.

There are two main disadvantages associated with LYSO scintillators: they offer only average light output, and they exhibit intrinsic radioactivity through  $\beta^-$  decay of  $^{176}\text{Lu}$  (half-life  $3.78 \times 10^{10}$  years) which results in two gamma photon emissions at energies 307 and 202 keV. [25] These photons are emitted from and often reabsorbed within the crystal, therefore inducing some intrinsic background scintillation light which degrades the 511 keV signal to noise ratio. However, LYSO crystal has overall superior performance characteristics compared to BGO and CsI and therefore, it is widely used in high-performing PET scanners.

The PET detector module includes a  $24 \times 24$  pixelated LYSO crystal array with overall dimensions  $57.66 \text{ mm} \times 57.66 \text{ mm}$  with a thickness of 13.00 mm (Figure 4). Each crystal pixel measures  $2.32 \text{ mm} \times 2.32 \text{ mm}$  and are separated by a specular reflector with thickness a of 0.08 mm. The specular reflector also covers the outside of the crystal array on all sides except for that which is bonded to the light guide so scintillation light may be funneled toward the photosensor. The light guide is tapered such that the top and bottom face match the dimensions of the scintillation crystal and photosensor respectively, creating a geometric match between the LYSO crystal size and the active area of the photosensor. [26]

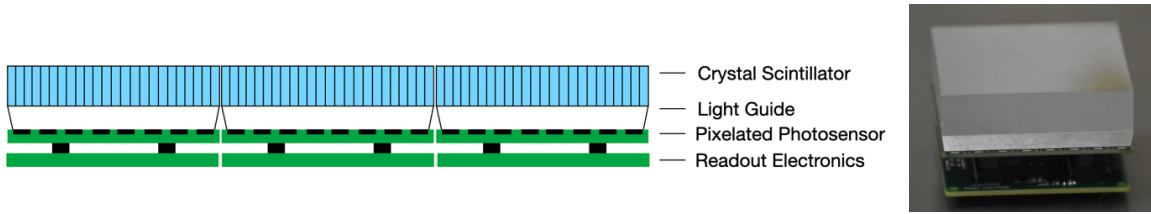


Figure 4. Left: 1-dimensional schematic presentation of the cross-section of three tiled detector blocks; Right: The photo of a block detector with crystal array wrapped in a light reflective material, tapered light guide and SiPMs array with an electronic board underneath.

The selected SiPM photosensors are the Array-C photodetector (ON Semiconductor, Pheonix, AZ) which consist of an  $8 \times 8$  pixelated array with an overall size of  $57.40 \text{ mm} \times 57.40 \text{ mm}$ , pixel pitch of  $7.2 \text{ mm}$ , and minimal inactive sensing area (dead space) between pixels. Each pixel is comprised of  $\sim 18980$  avalanche photodiode microcells which absorb photons to generate electron-hole pairs. They exhibit picosecond rise time and  $95 \text{ ns}$  microcell recharge time which allows for high count rate and precise timing capabilities required for organ-targeted PET applications.

Two adjustable parameters which are important for SiPM performance in the context of organ-targeted PET are bias voltage and operating temperature. As temperature is increased, so too is the voltage required to achieve breakdown  $V_{Br}$ , while signal gain is decreased as reported in Table 4. Additionally, the powerful thermal effect on charge carrier ionization results in increased dark current with rising temperature. Therefore, the tuning and maintenance of sensor operational temperature is critical for consistent and predictable detector response. The operational overvoltage has been optimized for signal gain, detection efficiency, and noise performance through experimentation at various combinations of bias and temperature settings made possible by the specialized electronics and detector cooling system described in 2.2.2.

Table 4. Summarized performance parameters for SensL ArrayC SiPM sensors at operational bias voltage.

Parameter	Typical Value
Peak absorption wavelength	420 nm
Spectral range	300-950 nm
Signal gain	$3 \times 10^6$
Photon detection efficiency	41%
Dark current	618 nA
Dark count rate	1200 kHz

Microcell recharge time constant	95 ns
Temperature dependence of $V_{Br}$	21.5 mV/ $^{\circ}$ C
Temperature dependence of gain	-0.8%/ $^{\circ}$ C
Crosstalk	7%
Afterpulsing	0.2%
Number of microcells per pixel	18980
Microcell fill factor	64%
Microcell size	35 $\mu$ m

The board connectors provide 64 fast outputs, 64 standard input/output (I/O), and 32 common I/O with summed cathode connections. Relevant performance parameters are reported in Table 4 for the ArrayC sensor with 35 $\mu$ m microcell size and  $V_{Br}$  specified at 24.7V.

Each SiPM sensor interfaces directly with a 4-channel preamplifier (AB4T-ARRAY64P, AiT, Newport News, VA) through board-to-board connections. The preamplifier encodes the photosensor signals via charge division which is multiplexed to four position signals for each detected event:  $X^+$ ,  $X^-$ ,  $Y^+$ ,  $Y^-$ . The monolithic light guide between the  $24 \times 24$  pixelated scintillator permits light sharing across the  $8 \times 8$  pixelated photosensor as seen in Figure 5, so detection event coordinates can be reconstructed from this 4-channel signal readout using Anger Logic [27]. Anger Logic describes a coordinate reconstruction process which decodes positional information from the weighted average or centroid of SiPM pixel signals based on the relative distribution of scintillation light (Figure 5). Calibrations for spatial nonlinearity are performed to compensate for effects produced at detector edges. The energy of the detected event is given by summing the coordinate signals. Dedicated acquisition electronics digitize voltage signals from the SiPMs corresponding to detected coincident events.

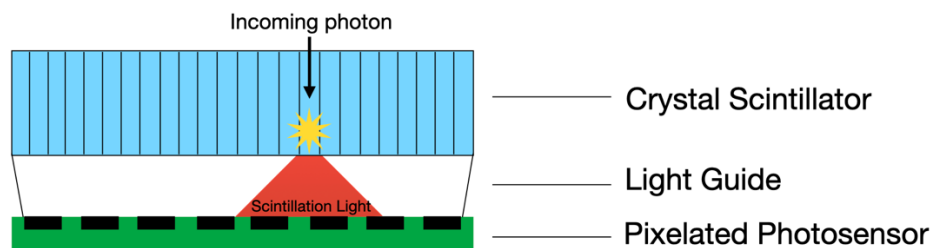


Figure 5. A 1-dimensional schematic showing scintillation light-sharing over multiple SiPM pixels using a monolithic light guide in response to gamma photon detection.

The developed PET technology was licensed to Radialis Inc. for production of a commercial scanner called the Radialis PET Camera. This clinical scanner serves as the hardware under study in subsequent sections.

### 2.2.1. Radialis Organ-Targeted PET Detector and System Design

The Radialis organ-targeted PET camera utilizes an adjustable detector configuration which creates versatility for imaging different organs including the breast, prostate, and heart. The system employs two planar detector heads mounted on a movable gantry (Figure 6). The detector heads are identical and comprised of twelve individual detector modules described above, which are seamlessly arranged in a 4×3 array to produce an active sensing area measuring 230.64 mm × 172.98 mm (Figure 7). The detector housing is made from a thin, durable composite material so that the imaging area is only ~4 mm from the edge of the detector housing.



Figure 6. Configuration of the Radialis organ-targeted PET Camera with two planar detector heads for positioning around an organ of interest.

The adjustable gantry permits positioning of the detectors proximal to the organ of interest. For breast imaging, patients are seated upright with the detector heads positioned on either side of the immobilized breast. A gantry with a rotation axis allows for 90-degree rotation of the detector heads clockwise and counter-clockwise from its starting position.

This permits acquisition of breast and axilla images at standard views (i.e., bilateral craniocaudal (CC) and mediolateral oblique (MLO) views) as well as at supplementary views if additional information is required. It also allows a technician to adjust the position and distance between the detector heads to accommodate the patient's height and breast size. Each movement stage consists of sensor elements and safeguards for patient and operator safety, with control via touch screen operator interfaces.

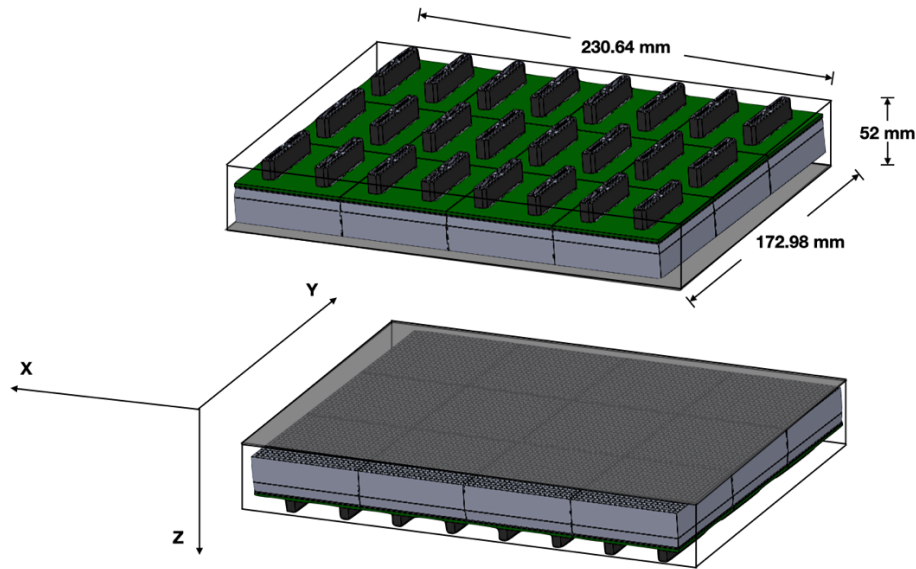


Figure 7. Detector schematic showing the overall size of the detector heads with 3x4 array of sensor modules per detector head and the axis convention for measurements.

### 2.2.2. Cooling

Thermal stability of the SiPMs is critical for ensuring consistent and predictable performance. This is achieved by actively cooling the detector arrays using a temperature control unit and maintaining the operating temperature of the detector head at  $15 \pm 0.5$  °C. This cooling approach allows for stable operation of the detector heads during ongoing image acquisition in a clinical setting.

The temperature control unit consists of a liquid chiller assembly, as well as a series of fans for cooling of internal electronics. The liquid chiller assembly provides coolant to radiators mounted adjacent to the SiPMs and their preamplifier printed circuit boards (PCBs) to regulate the temperature within the detector head. The radiators assemble between the sensor PCBs and the pre-amplifier PCBs, and a thermal pad provides the

interface between the radiator and the sensor PCBs to maximize heat conduction to the radiators.

The liquid chiller assembly is housed within the system and supplies coolant to radiators in both detector heads in a closed-loop system. It includes a coolant pump, chiller assembly with heat exchanger and compressor, temperature sensors and flow meter, and reservoir with coolant level sensing. Environment sensors within the detector heads relay information to a controller to ensure that the detectors remain at the specified operational temperature, and to alert should a high-humidity state occur, indicating a possible leak or condensation. To ensure no possible damage to electronic components, a special non-conductive coolant is used as well as real-time coolant level monitoring.

### **2.3. Data Acquisition**

The organ-targeted PET camera's data acquisition (DAQ) system serves to collect and process data needed to produce radiological images. Its function is based on coincident detection of antiparallel gamma photons which originate from a positron-emitting radiotracer within the system FOV. The DAQ system detects, registers, and process these coincident events before relaying this acquired data to a computer system for image reconstruction.

The DAQ electronics include a 24-input coincidence trigger module, six 16-channel analog to digital converter (ADC) boards and data switch module PCBs, 32-bit low voltage differential signaling (LVDS) bus to Gigabit data interface module, and six signal adapters each serving four 4-sum coordinate signals from the detector heads. The DAQ is designed to trigger, digitize, and transmit imaging data such that any pair of time-coincident scintillation signals will form a single "event". Events are composed according to the coincidence matrix programmed in the trigger unit and are aggregated and sent as 43 event user datagram protocol (UDP) blocks of 8192 binary bytes via the Gigabit module to the computer workstation for storage and image reconstruction.

#### **2.3.1. Analog to Digital Conversion**

The organ-targeted PET system uses 6 ADC modules, each with 16 channels, to record signals across the 24 detectors to reconstruct the location of a positron emission. Each ADC module features 12-bit analog to digital signal conversion and is specifically configured for use with the selected preamplifiers boards. All inputs feature active internal

50-ohm termination to prevent signal reflection. The trigger module provides an integration “gate” signal of defined width for which the total charge received on each analog input is converted to voltage and then converted to 12-bit data. This process is also subject to a 100ns analog delay line which is present in each channel. Under typical clinical imaging conditions, only a small subset of 96 ADC channels will have “non-background” data corresponding to useful imaging information. Radialis software is responsible for processing this data for image reconstruction. A summary of ADC parameters is given in Table 5.

Table 5. Summary of ADC module specifications for the Radialis PET Camera

Analog input impedance/polarity	50 Ohm/negative
Analog to digital conversion time	600ns typ.
ADC behavior upon saturation	Remains at high value
Usable charge integration width	30 - 3000 ns
Dead time due to data transfer	~0.35us per module

### 1.1.3. Coincidence detection

The DAQ system trigger module compares signals detected in each detector head for occurrence within a predetermined coincidence timing window. For the close detector separations used in organ-targeted PET, the coincidence timing window is set to 3 ns. If two events are detected within this window, they are deemed a coincidence event having originated from the same positron annihilation and the acquired ADC data is recorded. Summarized trigger module specifications are provided in Table 6.

Table 6. Summary of trigger module specifications for the Radialis PET Camera.

Coincidence timing window	3 ns
Input impedance	50 ohm
Input threshold range	20 – 200 mV
Output gate width adjustment range	30 – 500 ns
Coincidence map	Any signal from head “A” vs. any signal from head “B”
Dead time	3 μs

### **2.3.2. DAQ Event Processing**

The specially designed DAQ system permits high-throughput processing of detected events. System control signals are provided by the trigger module along with the “Gate” signals to the ADC modules. In order to minimize electromagnetic interference (EMI) between digital communication and the analog inputs, all high-speed data and control signals use low-noise LVDS standard.

The module has 24 analog inputs which are configured to accept positive input signals. Each channel features a fixed-ratio high/low two-discriminator scheme in order to optimize timing resolution. The low threshold defines time reference, and the high threshold acts as an “Enable” function. An internal field programmable gate array (FPGA) logic requires pairs of input signals to arrive within the coincidence timing window to generate gate signals to start the ADC modules. The width of the gate signal defines the charge-integration time for analog signal inputs and is common across all ADC modules.

The output logical signals correspond to signals received within the coincidence timing window on two inputs of the trigger module. This results in logical “High” outputs to the corresponding ADC modules for the duration of the gate signal. The trigger module will prevent starting an ADC module while the previous event is being processed. The time required to start and read all 6 ADC modules after registering a valid coincident event is considered the dead time, where the internal logic of the trigger module remains locked.

The gigabit module stores events in the buffer, once buffer acquires 43 events the data is sent to the computer for storage and image reconstruction. The gigabit module also supplies bias voltage to the SiPM photosensors via a board-mounted power supply unit.

### **2.3.3. Computer System and Data Storage**

The server computer uses a Linux operating system and receives incoming UDP packets of detected event data via direct ethernet connection. The computer aggregates the data in a dump file (dmp) during an imaging acquisition. All data is stored locally on the computer hard drive where the reconstruction software can perform processing to produce the final image. There are four unique ADC channels assigned to each block detector element in upper and lower detector heads termed A and B, with 16 channels corresponding

to each of the six ADC modules. The ADC channels for each module are assigned as in Figure 8. The resultant dmp file consists of 96 channels with each event corresponding to 192 bytes of data.

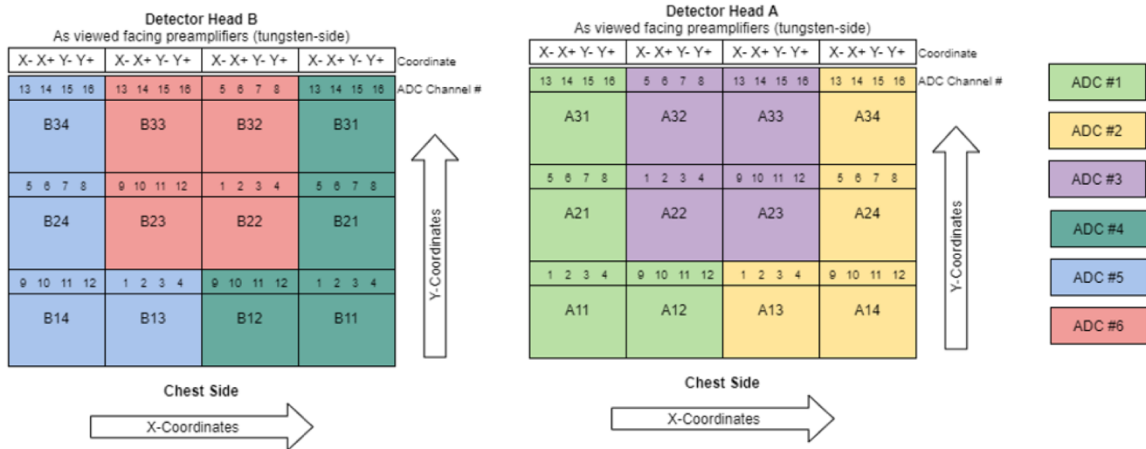


Figure 8. Block detector channel assignments with corresponding ADC for the purpose of decoding event coordinates for upper and lower detector heads A and B.

## 2.4. Image Reconstruction

The image reconstruction workflow consists of the set of programs developed to convert raw binary data from the PET DAQ system into list-mode data, perform image reconstruction on the corresponding list mode data, and convert reconstructed data into a digital imaging and communications in medicine (DICOM) image. The programs within the reconstruction workflow were implemented in Python and MATLAB programming languages and the reconstruction algorithm was implemented in C++ programming language.

### 2.4.1. Reconstruction Algorithm

Maximum likelihood expectation maximization (MLEM) is used for the Radialis PET image reconstruction. MLEM uses a statistical model to estimate the distribution of the radiotracer in the body from initial projection data, considering the physical properties of the scanner and the radiotracer being used to iteratively refine the estimate until it converges to a stable solution. The MLEM algorithm is based on the maximum likelihood principle, which states that the most likely estimate of a parameter is the one that maximizes the likelihood of the observed data, given that parameter. In the case of PET imaging, the

parameter of interest is the probability distribution of the tracer in the body, and the observed data is the projection data.

The algorithm begins with an initial estimate of the probability distribution, which is typically uniform or based on prior knowledge of the tracer distribution from back-projection of coincident events. The algorithm then simulates the expected projection data based on this initial estimate and compares it to the actual measured projection data. The difference between the simulated and measured data is used to update the estimate of the probability distribution. This process is repeated iteratively until the difference between the simulated and measured data is minimized, and the estimate of the probability distribution converges to a stable solution.

The MLEM algorithm is effective at handling noise and other sources of uncertainty in the imaging data and can result in better resolution than images produced by back-projection reconstruction. Back-projection is a relatively simple algorithm which projects coordinate data from detected coincident events back into image space based on LORs drawn between the corresponding detector coordinates. Another advantage is that MLEM can be used to correct for attenuation and scatter by incorporating these effects into the statistical model used for image reconstruction, minimizing these significant sources of error in PET imaging. However, the MLEM algorithm is computationally intensive and can be slow, particularly for large datasets. Overall, MLEM is able to improve resolvability of small details in reconstructed images and is the algorithm of choice for the organ-targeted PET application.

The number of MLEM iterations is a user-defined parameter which determines how long the algorithm will run and to what extent the estimate will be refined. The default clinical reconstruction algorithm for the organ-targeted PET scanner is set to run 15 iterations, meaning that it will perform the estimation and update process 15 times before stopping and producing the final reconstructed image. The selected number of iterations depends on various factors, including the complexity of the imaging data, the desired image quality, and the computational resources available. In general, increasing the number of iterations can improve the quality of the reconstructed image, but it also increases the computational cost and may enhance image noise. Here, the number of iterations was selected as it maximized visualization of small objects in the clinical setting. A median root

prior (MRP) filter is applied within the reconstruction pipeline [28] to correct nonuniformity produced by the MLEM algorithm. Reconstructed images are saved in DICOM format with 24 axial image slices of the XY plane. The image matrix is defined by a pixel size of 0.4 mm × 0.4 mm. The voxel dimension is determined by the detector separation divided into 24 equal components and may vary among acquisitions depending on the detector separation used during image acquisition.

It is worth noting that the MLEM algorithm is just one of many iterative algorithms that can be used for PET image reconstruction. Other popular iterative algorithms include the ordered subsets expectation maximization (OSEM) algorithm and the maximum a posteriori (MAP) algorithm. Each algorithm has its own strengths and weaknesses and can be tuned to produce different types of images based on the specific imaging data and application.

## **2.5. PET Data Integrity**

To ensure an accurate reconstruction of activity distributed within a patient, detected PET events should correspond to two 511 keV photons which have originated from the same positron annihilation and emerged from the region of interest without any interactions prior to detection. From this, an assumption is made that the photons originated from a positron annihilation which occurred at some point along the line drawn between the detected photon coordinates.

### **2.5.1. Energy Filter**

Detected coincident events undergo an initial filtration step to remove data which corresponds to scattered 511 keV photons. Since annihilation photons which undergo Compton scattering will lose a portion of their initial energy, it is possible to preferentially select for non-scattered photons by filtering out those which are detected below 511 keV. In doing so, the accuracy of the LORs used for image reconstruction will correspond to the true sites of positron annihilation. However, since the PET detectors exhibit a finite energy resolution, true 511 keV photons will be measured with a distribution of energies centered around, but not discretely at, 511 keV. Therefore, an energy filter or window is configured to accept photons with energies measuring between 350 keV – 700 keV. While a narrower window of acceptance will minimize the contribution of slightly scattered photons in the

reconstructed image, it also significantly reduces the total number of counts and may degrade reconstructed image quality due to reduced statistics. Image quality evaluation for resolvability of small details has informed the use of this default energy filter for the clinical reconstruction workflow.

### **2.5.2. Angular Filter**

In addition to the energy filter, an angular or LOR angle allowance filter is implemented to reject events within the list-mode data based on the endpoints of each LOR. If the difference between the coordinates of detected coincident events in the XY plane is larger than a predefined threshold, the event is discarded from further processing. This discriminates oblique LORs and thus reduces the contribution of parallax effect shown in Figure 3. This produces error in LOR assignment and inaccuracies in image reconstruction. The angular filter ensures data integrity by discarding coincidence events which are at angles greater than 1 radian from the detector surface based on the two LOR endpoint coordinates since these events have a higher likelihood of multiple crystal pixel interaction.

### **2.5.3. Attenuation Correction**

In PET, the probability of event detection decreases with attenuation in the media, but this effect does not depend on the actual position of positron annihilation along the LOR. Thus, attenuation can be calculated based on the total lengths of LOR within the FOV. The organ-targeted PET Camera has no transmission data available, so the organ shape identification is performed by image segmentation and correction for the predicted tissue attenuation is applied.

The attenuation correction first requires reconstruction of an uncorrected image from the acquired data. Since tissue within the FOV produces significantly more contrast than air, the boundary of an organ such as the breast can be identified relative to air and the uncorrected image is segmented to define the shape of the organ based upon this boundary. Breast tissue does not contain hard structures such as bone, so segmented image voxels are corrected for linear attenuation coefficients of soft tissue inside the organ boundary ( $0.098 \text{ cm}^{-1}$ ) and for air outside the organ ( $1.04 \times 10^{-4} \text{ cm}^{-1}$ ). The corrected image is supplied to the MLEM reconstruction algorithm, and a new image is produced.

#### **2.5.4. Scatter Correction**

In contrast with conventional WB PET/CT, the organ-targeted PET system does not benefit from an x-ray transmission source to measure the attenuating properties of tissue. Because of this, scatter corrections are performed by the Estimation of Trues Method (ETM). This method is based on the measured energy of detected photons and the assumption that the percentage of scattered events in a higher energy window is lower relative to this percentage in the standard energy window. To implement the ETM, an image is reconstructed with photons passing the standard energy filter (350 keV – 700 keV). A second image is reconstructed from the same data but now excluding photons below 500 keV (500 keV – 700 keV). The second image is scaled to match the number of un-scattered events in the first image and subtracted from the first image leaving only an image of scattered events. Image smoothing is applied, and this image of scattered events is subtracted from the original image, thereby subtracting image noise due to scattered photons.

### **3. Standardized Imaging Evaluation of an Organ-Targeted PET Camera**

The following section contains content published in *Sensors*, entitled: Stiles, J.; Baldassi, B.; Bubon, O.; Poladyan, H.; Freitas, V.; Scaranelo, A.; Mulligan, A.M.; Waterston, M.; Reznik, A. Evaluation of a High-Sensitivity Organ-Targeted PET Camera. *Sensors* 2022, 22, 4678. <https://doi.org/10.3390/s22134678>

Stiles and Baldassi are the first authors who contributed equally to the presented research.

This section presents the evaluation of imaging performance for the Radialis PET Camera conducted in accordance with the National Electrical Manufacturers Association (NEMA) NU-4 standards. The results are compared with other organ-targeted, WB PET/CT, and total body PET/CT scanners which are currently in clinical use or undergoing clinical trials. The performance of the scanner is evaluated considering the critical need to reduce the radiotracer dose and thus radiation exposure associated with diagnostic PET imaging.

### 3.1. Introduction

Currently, the average standard-of-care  $^{18}\text{F}$ -FDG radiotracer dose for both WB PET/CT and organ-targeted PET examinations is 370 MBq, which results in an effective dose from PET scanning of  $\sim 6$  mSv [29]. Even though organ-targeted PET significantly reduces the effective dose compared to PET/CT due to elimination of the CT component (which accounts for  $\sim 50\%$ – $80\%$  of the total combined patient dose during PET/CT, to a lesser extent with low-dose CT attenuation correction [29]), PET radiotracers still deliver  $\sim 5$  times more effective dose than, for example, x-ray mammography [30, 31]. The large radiation dose associated with PET limits its use in undiagnosed patients, such as in disease screening applications for which there is increasing justification. Another limitation which restricts widespread adoption of organ-targeted PET are gantry geometries which constrain use to a single target organ, where a versatile design may permit higher rates of utilization by extending use to other organs.

Organ-targeted PET has the potential to significantly impact breast cancer imaging by addressing the need for early detection in women with radiologically dense breasts. Since PET imaging is not dependent on tissue density, it can offer a solution for women who are at high risk of cancer and for whom conventional x-ray mammography is ineffective due to radiologically dense breast tissues. However, to be considered as a screening alternative to x-ray mammography and breast MRI, organ-targeted PET detectors must be capable of imaging at significantly lower doses. Ideally, a 10-times dose reduction is needed to radically expand patient populations for whom PET is an appropriate imaging modality. This includes women at high risk of breast cancer development, pediatric patients, and patients who require multiple nuclear medicine examinations such as during evaluation of treatment response. Overall, although organ-targeted PET has the potential for new advances in diagnosis and theragnostic procedures, from cancer to cardiac and neuroimaging [32], a significant improvement in PET detector sensitivity is required so that the relatively high whole-body radiation exposure is reduced [33, 34, 35, 36].

The aim of this study is to evaluate the design and performance of a clinical organ-targeted PET camera [26, 37, 38] and its ability to address the above problems. The PET technology described here was intentionally designed to provide high resolution and high detection sensitivity to maximize the signal from a positron-emitting radiotracer. The Radialis

organ-targeted scanner is dedicated to breast imaging in what is sometimes referred to as Positron Emission Mammography (PEM), by analogy with conventional x-ray mammography. The scanner consists of two planar PET detector heads (each with FOV 174 mm × 232 mm, comparable to digital x-ray mammography systems) which are positioned on either side of an immobilized (i.e., not compressed) breast (Figure 6). The large FOV arranged proximal to the breast maximizes signal detection by providing large solid angle coverage while also reducing detection of signal from elsewhere in the body. This results in improved signal-to-noise ratio and greater image contrast. Also, improved signal detection may shorten exam times, thus improving patient comfort, minimizing motion artifacts, and increasing patient throughput. The modular technology also offers a flexible geometry which may be adapted for other possible indications [33].

The standardized tests are intended to assess the system's imaging characteristics in terms of activity sensitivity, count rate performance, and spatial resolution. These parameters are evaluated according to NEMA NU-4 standards [39], with modifications to accommodate the planar detector design of the PET camera. The detectability of small objects was assessed with Micro Hotspot phantom images, and spatial resolution was measured per NEMA protocols. The system count rate performance and scatter fraction are assessed using a cylindrical scatter phantom, and overall efficiency at peak NECR is determined. Finally, the system sensitivity is measured per NEMA protocols. The results of standardized measurements are compared with other commercially available organ-dedicated and WB PET scanners.

## **3.2. Spatial Resolution**

### **3.2.1. Methods**

The performance was evaluated according to NEMA NU-4 2008 [39] standard for pre-clinical scanners since this closely resembles the FOV of the Radialis organ-targeted PET scanner. Spatial resolution was measured by imaging a point source of radioactivity at discrete positions across the FOV in XY and Z axes as shown in Figure 7 ( $^{22}\text{Na}$  source with 0.3 mm diameter encased within an acrylic cube measuring 10 mm × 10 mm × 10 mm). The detector heads were separated by 80 mm and measurements were acquired from the center of the FOV across the XY plane (i.e., from  $x = 0$ ,  $y = 0$ ,  $z = 40$  mm), and repeated at one-quarter axial offset ( $z = 20$  mm).

The original activity of the  $^{22}\text{Na}$  source was 111 kBq (3  $\mu\text{Ci}$ ) and the calibrated activity of the source during these experiments was determined to be 89.9 kBq. No background radioactivity was used for point source measurements. Each measurement was calibrated to run until more than 100,000 prompt counts were acquired, and the list-mode data was processed according to NEMA NU-4 – 2008 protocols with a single slice re-binning (SSRB) reconstruction method [40,41]. This method assigns a coordinate to each LOR which intersects the image plane halfway between the detector surfaces. Profiles of each source were created in ImageJ [42] by plotting through the maximum intensity pixel of the source and measuring the image gray value along that line. An image pixel size of 0.2 mm for the XY plane and a voxel depth of 2.67 mm was used for the image matrix size throughout the analysis.

Spatial resolution is reported as FWHM and full width at tenth maximum (FWTM) of the point spread function (PSF) derived using a gaussian fit to the data reconstructed with the clinical iterative MLEM algorithm. The system is calibrated using a flood scan uniformity acquisition. No other corrections are applied to these data sets, such as scatter, attenuation, or dead-time corrections. Here, we followed a widely adopted practice for PSF characterization [43,44,45] although this slightly deviated from NEMA NU-4 requirements that derives FWHM from line profiles drawn through the image of the point source. Resolution was quoted for each axial direction as either X, Y, or Z resolution corresponding to the direction of the profile across the image.

### **3.2.2. Results**

The spatial resolution as a function of point source location is presented in Figure 9 and Table 7 showing the X, Y, and Z resolutions as functions of activity location using MLEM reconstruction. The average in-plane spatial resolution in X and Y is measured to be  $2.3 \pm 0.1$  mm. As a result of the planar geometry and lack of multiple acquisition angles, the cross-plane or Z resolution of the system is about three times larger than in-plane resolution and has an average value of  $6.8 \pm 0.7$  mm within the central FOV.

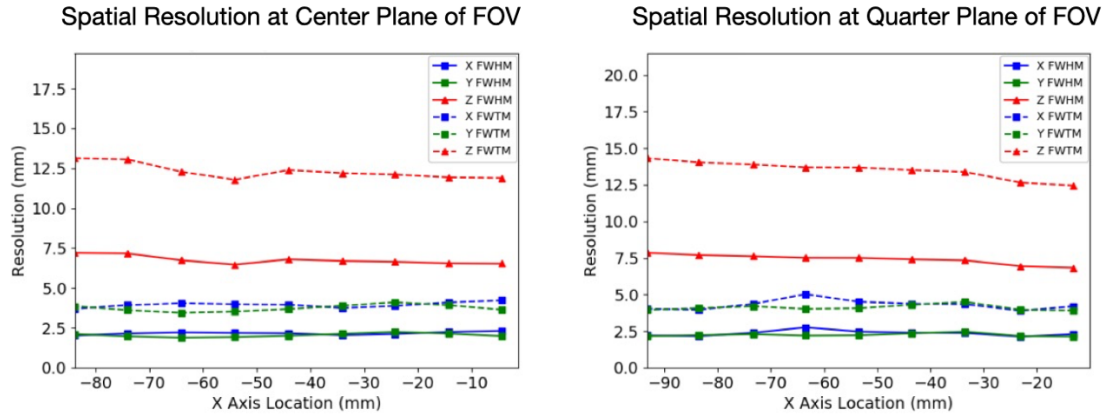


Figure 9. Reconstructed system spatial resolution of a Na-22 point source measured per NEMA protocols with a MLEM reconstruction algorithm. Left: The central Z Axis resolution plotted as a function of point source location along the X Axis. Right: Quarter Z Axis resolution plotted as a function of point source location along the X Axis.

The in-plane system spatial resolution significantly outperforms WB PET scanners and is comparable to other organ-dedicated PET systems [44, 46]. Unlike anatomical imaging such as CT, PET imaging performance as a molecular imaging modality is not only governed by spatial resolution of point sources. Therefore, subsequent measurements serve to provide a more complete understanding of the system’s imaging capabilities.

Table 7. Summary of measured FWHM and FWTM spatial resolution in for a detector head separation of 80mm using MLEM reconstruction.

	X axis		Y axis	
	FWHM	FWTM	FWHM	FWTM
<b>Resolution at Z=0 mm</b>				
<b>In-plane X (mm)</b>	2.2±0.1	4.1±0.2	2.4±0.2	4.4±0.4
<b>In-plane Y (mm)</b>	2.2±0.1	4.1±0.2	2.3±0.1	4.1±0.1
<b>Cross-plane Z (mm)</b>	7.8±0.3	14.2±0.5	6.6±0.9	12.1±1.7
<b>Resolution at Z=20 mm</b>				
<b>In-plane X (mm)</b>	2.4±0.2	4.3±0.3	2.5±0.1	4.5±0.1
<b>In-plane Y (mm)</b>	2.2±0.1	4.1±0.2	2.2±0.2	4.1±0.3
<b>Cross-plane Z (mm)</b>	7.3±0.5	13.3±0.9	6.9±0.6	12.7±1.0

### 3.3. Sensitivity

#### 3.3.1. Methods

A  $^{22}\text{Na}$  point source was also used for evaluating system detection sensitivity to 511 keV annihilation photons. The source was positioned in the center of the XY plane, halfway along the Z-axis between detectors separated by 60 mm. Acquisitions of coincidence data

were performed for 60 seconds at each of 113 discrete positions separated by 2 mm. Each acquisition was reconstructed with an SSRB image processing algorithm. Values of the axial sensitivity  $S_i$  and the absolute per-slice slice sensitivity  $S_{A,i}$  [39] were determined and plotted as a function of source location in the FOV.

Equation 9

$$S_i = \frac{R_i - R_{B,i}}{A_{Cal}}$$

Equation 10

$$S_{A,i} = \frac{S_i}{0.9060} \times 100$$

where  $R_i$  is the count rate measured for slice  $i$ ,  $R_{B,i}$  is the background count rate for slice  $i$ , and  $A_{Cal}$  is the calibrated activity of the source. Absolute sensitivity was calculated with the branching ratio of  $^{22}\text{Na}$  (ie: 0.9060) and the calculated sensitivity  $S_i$  for slice  $i$ . The average system sensitivity was determined as the mean sensitivity of discrete points measured across the FOV.

### 3.3.2. Results

System sensitivity measurements are presented in Figure 10 as a function of point source position along the X-axis. The system achieved a peak axial sensitivity of 32 cps/kBq at the center of the FOV with 60 mm detector separation. The peak absolute sensitivity is 3.5% and the total average system sensitivity is 2.4%. The sensitivity gradually decreases as the source is moved towards the edge of the detector head since an increasing number of LORs will escape detection due to lesser solid angle coverage.

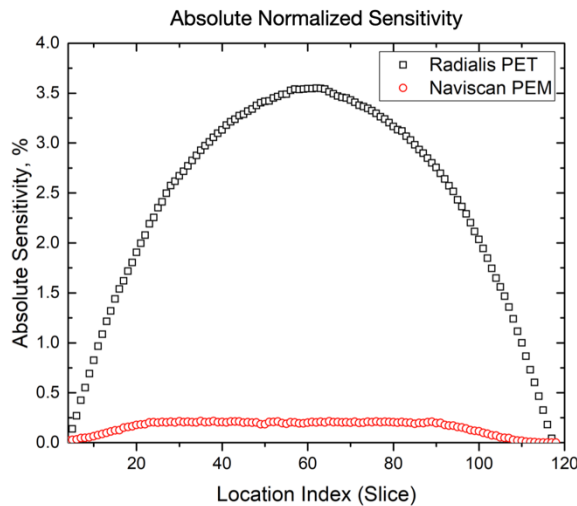


Figure 10. Axial absolute sensitivity plotted against point source location along the X axis for the Radialis PET and Naviscan PEM Flex Solo II scanner<sup>44</sup>.

In comparison with other commercially available organ-dedicated scanners, the detector design and geometry described here results in improved absolute sensitivity to detection of 511 keV annihilation photons [44, 46]. Although ring geometries of other scanners show nominally higher point source resolution than the Radialis PET Camera (1.5-1.9 mm [47] vs. 2.2-2.4 mm), the sensitivity for identifying clinically relevant cancers is highly dependent on the overall efficiency of tracer detection and a scanner's ability to recover contrast. The ring geometry used by other scanners is also limited in its ability to detect contrast enhancement near the chest wall [48]. The significantly improved detection sensitivity achieved by the Radialis PET Camera is critical for enabling clinical imaging at low doses of radiotracer.

### 3.4. Count Rate Performance

#### 3.4.1. Methods

A NEMA NU-4 scatter, or rat, phantom was used to measure count rate statistics. The phantom consists of a cylindrical high-density polyethylene (0.98 g/cm<sup>3</sup>) with a diameter of 50 mm and a length of 150 mm. The line source consists of a cylindrical cavity with a diameter of 3.5 mm drilled lengthwise through the phantom at an axial offset of 17.5 mm and filled with 51 MBq of <sup>18</sup>F solution. The line source was closed at each end with 4 mm long syringe ports, resulting in an overall length of 142 mm.

The phantom was placed at the center of the XY FOV ( $y=0$ ) parallel to the X axis halfway between the detector heads in Z with a separation of 60 mm. Acquisitions began immediately after the phantom was filled and were programmed to repeat every 15 minutes until the phantom had decayed through 10 half-lives and a maximum of 29 million total events had been acquired. Negligible activity remained in the final acquisitions.

Data processing for count rates involved reconstructing list mode acquisition data files using LOR acceptance angle filtration. The resulting files were then processed using an SSRB image reconstruction technique. Peak count rates were determined from the plots of count rates vs phantom activity concentration.

NECR performance was evaluated over a clinically relevant activity range and efficiency at peak noise equivalent count rate was determined as the peak NECR normalized to the activity at the peak:

Equation 11

$$Eff_{NECR,peak} = \frac{NECRR_{peak}}{A_{peak}}$$

### 3.4.2. Results

System count rates are plotted against the scatter phantom activity concentration in Figure 11 and summarized in Table 8 with a variety of LOR angle acceptance filters. Activity concentrations corresponding to specific standard uptake values (SUV) are marked on each count rate plot and are calculated for different clinically relevant injected activities in a 77.3 kg woman. The values of SUV = 1 are included to estimate the background tissue activity concentrations expected during clinical acquisitions. Peak NECRs were achieved at a phantom activity concentration of 10.5 kBq/mL with an efficiency at peak NECR of 5,650 cps/MBq.

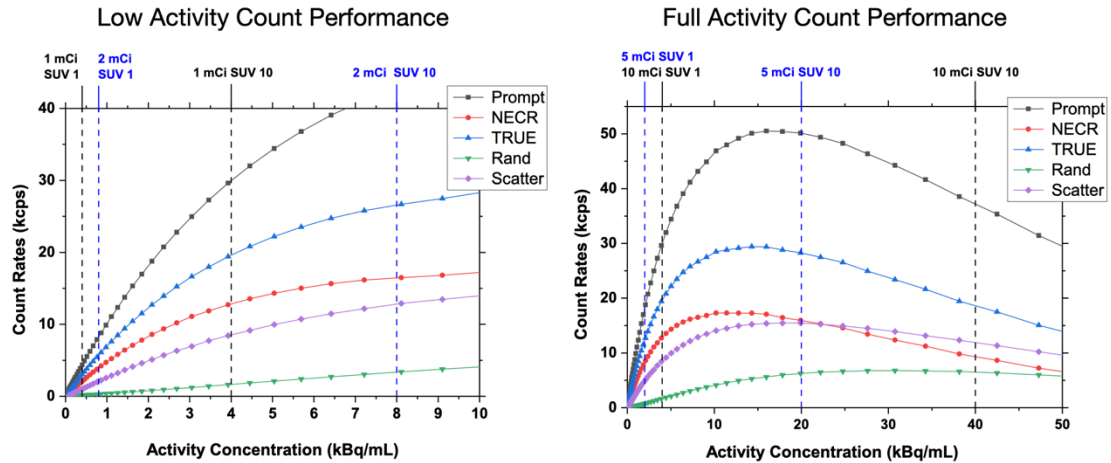


Figure 11. System count rate curves for low and full activity concentrations.

The scatter fraction for the 90 mm and 110 mm LOR angular filters are 24% and 31% respectively. Use of a 52 mm LOR angle allowance filter further reduces the scatter fraction to 6.2% accompanied by a cut to the overall count rates.

Table 8. Summarized values for count rates at different LOR angle allowance parameters.

	60 mm Angle Allowance (k cps)	90 mm Angle Allowance (k cps)	110 mm Angle Allowance (k cps)	144 mm Angle Allowance (k cps)
Peak NECR	9.6	17.3	17.8	18.1
Peak True Rate	13.8	28.5	32.5	36.4
Peak Prompt Rate	19.7	46.9	59.3	73.1
Peak Scatter Rate	4.15	13.9	20.9	29.3
Peak Random Rate	1.63	4.35	5.76	7.31

Despite design characteristics which make the Radialis PET Camera suitable for low-dose imaging, Figure 11 illustrates that the coincidence count rate capabilities and the dead time characteristics are still favorable for standard clinical doses. The equivalent SUV values are indicated for a standard clinical range of injected activity from 185 to 370 MBq (5 to 10 mCi), as well as low-dose 37 MBq (1 mCi) imaging. For SUV 1-7 at 370 MBq the count rates are no worse than 78% of the peak NECR. It is presumed that administered activity may be reduced without significant compromise in imaging results, by way of the higher sensitivity and low activity count rate peaks.

NECR describes the true coincidence rate that would give the observed signal to noise ratio (SNR), or the same level of statistical noise, if there were no random or scattered events detected. The Radialis PET camera exhibits much higher efficiency at peak count rate when compared to current WB systems [49,50,51]. The increased axial extent of the detectors and the absence of dead zones between modules provides superior geometric coverage of the organ being imaged and therefore more efficient detection of annihilation events than in other PET systems dedicated to imaging the breast (i.e., Oncovision Mamm PEM and Naviscan PEM Flex Solo II).

### **3.5. Micro Hotspot Phantom**

#### **3.5.1. Methods**

The micro hotspot phantom was used for the qualitative assessment of system resolution through the visualization of its small rods. The phantom was filled with 1 MBq of  $^{18}\text{F}$ -FDG and acquired for 40-minutes with a detector head separation of 89 mm, which was dictated by the phantom size. The phantom was immobilized by the detector heads and placed centrally in the X and Y directions. For image reconstruction, a pixel size of 0.2 mm  $\times$  0.2 mm was used to allow for visualization of smaller details. Post processing of the micro hotspot phantom was implemented in ImageJ with a 3D gaussian blur (sigma = 1.0 pixels) and with an unsharp mask (sigma = 7.0, mask weight = 0.6).

#### **3.5.2. Results**

The image of the Micro Hotspot phantom in Figure 12 was reconstructed using the clinical MLEM algorithm and demonstrates the visualization of small details down to the 1.35 mm diameter rods. This phantom image provides a more clinically relevant assessment of resolvability of small, tightly spaced objects, which may be encountered in clinical applications where background activity is present.

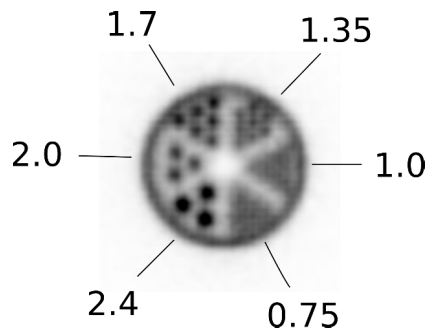


Figure 12. Image of the micro hotspot phantom reconstructed using MLEM reconstruction algorithm.

### 3.6. Summary

The developed PEM system has been extensively tested using phantoms containing the clinical radiotracer  $^{18}\text{F}$ -FDG. Spatial resolution was measured to be  $2.3 \pm 0.1$  mm for the in-plane resolution and  $6.8 \pm 0.1$  mm for the cross-plane resolution using default MLEM reconstruction algorithm. The maximum axial sensitivity achieved was 3.5%, with an average system sensitivity of 2.4%. The system peak noise equivalent count rate was 17.8 kecps at a  $^{18}\text{F}$ -FDG concentration of 10.5 kBq/mL. The overall efficiency at the peak noise equivalent count rate was 5,400 cps/MBq with a system scatter fraction of 24%. The detectability of small objects was shown with Micro Hotspot phantom images, as the 1.35 mm diameter rods were visualized. The evaluation indicates that the Radialis PET Camera is a promising technology for achieving high image quality organ-targeted PET imaging. The results have demonstrated superior sensitivity over available systems in this class, and this high-efficiency radiotracer detection creates an opportunity to reduce administered doses of radiopharmaceuticals and, therefore, patient exposure to radiation. Improved detector sensitivity will also permit a reduced scanning time required to both minimize the risk of motion artifacts and improve patient's throughput – an important element for making PET procedures cost-effective [52].

#### **4. Clinical Performance Demonstration of Organ-Targeted PET Camera**

The following section contains content published in *Sensors*, entitled: Baldassi, B.; Bubon, O.; Poladyan, Stiles, J.; H.; Freitas, V.; Scaranelo, A.; Mulligan, A.M.; Waterston, M.; Reznik, A. Evaluation of a High-Sensitivity Organ-Targeted PET Camera. *Sensors* 2022, 22, 4678. <https://doi.org/10.3390/s22134678>

Baldassi is the first author.

This section presents the evaluation of clinical imaging performance for the Radialis PET Camera conducted within the framework of a clinical study at the Princess Margaret Cancer Centre of the University Health Network (UHN-PMCC) in Toronto, Canada. The performance of the scanner is evaluated under a variety of clinical imaging conditions. including at 1/10 of the standard activity of  $^{18}\text{F}$ -FDG. The imaging results are compared with digital mammography, breast MRI, and WB PET scanners currently in clinical use.

#### **4.1. Introduction**

Organ-targeted PET imaging has the potential to address well-known limitations in breast cancer imaging. However, clinical integration requires radiation dose reduction to doses equivalent or lower than tomosynthesis and digital mammography (1.2 mSv and 0.5 mSv, respectively). The Radialis organ-targeted PET system has demonstrated high-sensitivity radiotracer detection and promise in its potential to reduce radiation dose and even time required per scan. These advancements are key to making PEM cost-efficient and to enable routine clinical use for women at high risk for breast cancer. Major prospective clinical applications for organ-targeted PET include supplementary screening when conventional x-ray mammography is suspicious but inconclusive, and primary screening for patients at higher-than-average risk of breast cancer for whom conventional x-ray mammography is inefficient.

Clinical validation and direct comparison with other imaging modalities is necessary to understand the capabilities and limitations of the Radialis PET technology. This study serves to validate the imaging performance which was previously evaluated through phantom measurements by providing comparative assessment under clinical imaging conditions in-vivo. The scanner is used to image breast cancer patients at standard WB activity and at 1/10 of the standard  $^{18}\text{F}$ -FDG activity. The acquired organ-targeted PET images are compared with other modalities for lesion detectability and specificity.

#### **4.2. Methods**

Image acquisition was performed at varying injected doses of  $^{18}\text{F}$ -FDG for biopsy-confirmed breast cancer patients (N=36, 33 – 85 years) [53] and images were reconstructed using the default clinical image reconstruction algorithm. Participants with a newly diagnosed breast cancer were injected with  $^{18}\text{F}$ -FDG activities between 37 and 307 MBq (activity was chosen randomly and did not depend on the clinical case) and an uptake period of 60 minutes was allocated for each participant prior to image acquisitions. An optional second image set was acquired for patients who opted to return for a subsequent imaging session where the  $^{18}\text{F}$  activity has decayed to approximately 1/4 of the initial activity (~4 hours post-injection).

Some participants were imaged with a Siemens Biograph Vision WB PET/CT scanner (image acquisition time ~30 minutes) on the same day prior to undergoing the organ-targeted

PET scan (image acquisition time ~ 5 minutes). The acquisition of both WB-PET/CT and Radialis organ-targeted PET images permits direct comparison between the two PET imaging modes. For some patients for whom WB PET/CT was not indicated, they were imaged with Radialis PET system and another breast imaging modality alone or in combination (i.e., FFDM, FFDM-DBT, MRI) prior to the PET scan within the clinical workflow. Imaging results were evaluated by radiologists and the findings are qualitatively compared for image quality and small lesion detectability.

### 4.3. Results

Clinical images acquired with the organ-targeted PET scanner are presented in Figure 13 compares full field digital mammography (FFDM) craniocaudal (CC) view (Figure 13, A) with a low-dose organ-targeted PET image also in CC view (Figure 13, B) acquired in a 56-year-old female with histopathology diagnosed invasive ductal carcinoma and intermediate-grade ductal carcinoma in situ (DCIS). For the PET imaging, the patient received intravenous 37 MBq of  $^{18}\text{F}$ -FDG, and the scanning was performed 1 hour after injection. The focal uptakes visible in the organ-targeted PET image (arrow and arrowhead in the Figure 13, B) corresponded to one mass (arrow Figure 13, A) detected on FFDM, however the other mass that was also histopathology proven as cancer was detected only in organ-targeted PET images. The second cancer was not detected by mammography, even in retrospect, because of the dense breast tissue masking effect.

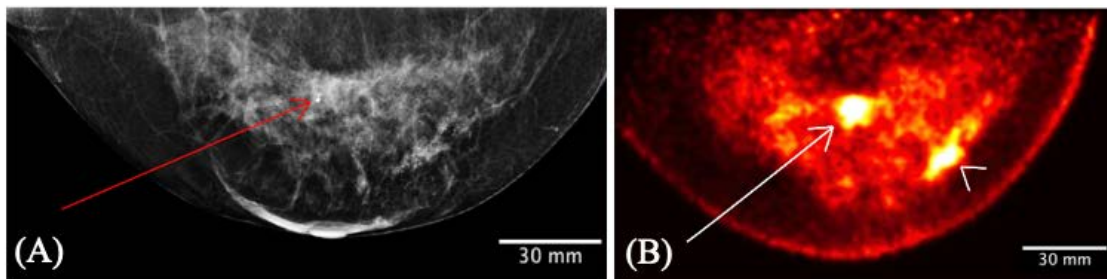


Figure 13. A 56-year-old female with invasive ductal carcinoma and intermediate-grade DCIS. Digital mammography of right breast (A) and right breast Radialis PET image with 37 MBq  $^{18}\text{F}$ -FDG injection (B) both in the same projection (CC view) are presented for comparison between these two imaging modalities. Cancers are demonstrated by the arrows (A, B) and arrowhead (B). The second cancer (arrowhead) is visualized only by Radialis PET (B).

The clinical image set in Figure 14 shows the comparison among multimodality images, specifically a FFDM CC view (Figure 14, A), MRI axial subtracted view (Figure 14, B), and two organ-targeted PET camera CC view images (Figure 14, C, D) obtained of a 61-

years old female patient with a known malignant disease involving the lateral aspect of the right breast. For the organ-targeted PET acquisition, 178 MBq of  $^{18}\text{F}$ -FDG was administered and two subsequent imaging sessions were acquired at 1 hour (Figure 14, C) and 4 hours (Figure 14, D) post injection. The PET images showed that changes in image contrast with time as activity decreases were not impactful for the radiologist visual assessment of multifocal cancers. Both PET images demonstrate  $^{18}\text{F}$ -FDG uptake in the extensive area that corresponds to the irregular mass detected on digital mammography and to a single irregular shape mass demonstrated by MRI images. However, the PET images are more reproducible of histopathology findings with multiple foci of cancers. Even after 4 hours, the PET image (Figure 14, D) still shows multiple distinct regions of increased uptake spanning an area of contiguous contrast enhancement on MRI or distortion on FFDM images.

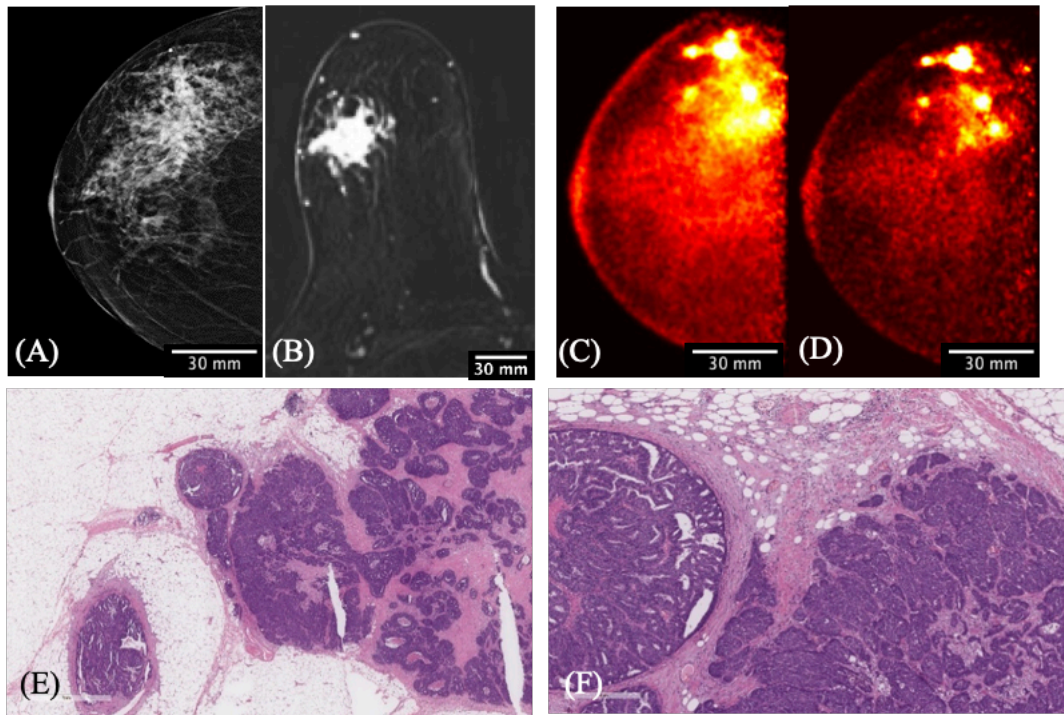


Figure 14. A 61-year-old female with right breast multifocal invasive and in situ ductal carcinoma. Images of the same breasts in: A) FFDM in the CC plane showing extensive distortion; B) a selected slice of MRI in the axial plane showing one irregular shape enhancing mass lesion after 2 min post gadolinium-chelates based contrast administration; C) 3D Radialis PET in the CC plane where multiple distinct regions of contrast uptake after 1 hour of 178 MBq  $^{18}\text{F}$ -FDG injection are evident; D) 3D Radialis PET in the CC plane where the conspicuity of the multiple regions of enhanced  $^{18}\text{F}$ -FDG uptake (indicative of multifocal cancers) remains after 3 hours from the prior (C) acquisition; E) invasive carcinoma in the center of the field with in situ carcinoma present at the periphery in pathology of mastectomy specimen; F) higher power view demonstrating intermediate grade invasive carcinoma on the right and papillary ductal carcinoma in situ on the left.

The clinical images in Figure 15 show the results of FFDM and organ-targeted PET imaging in a 50-years-old female patient with a palpable breast lump against the chest wall. The mediolateral oblique (MLO) digital mammography image identified a single palpable mass (red circle, Figure 15, A). PET camera images were acquired with 200 MBq of injected activity, revealing two additional regions of enhanced contrast along the patient's chest wall (Figure 15, B), which surgical pathology confirmed as malignancy (Figure 15, C, D).

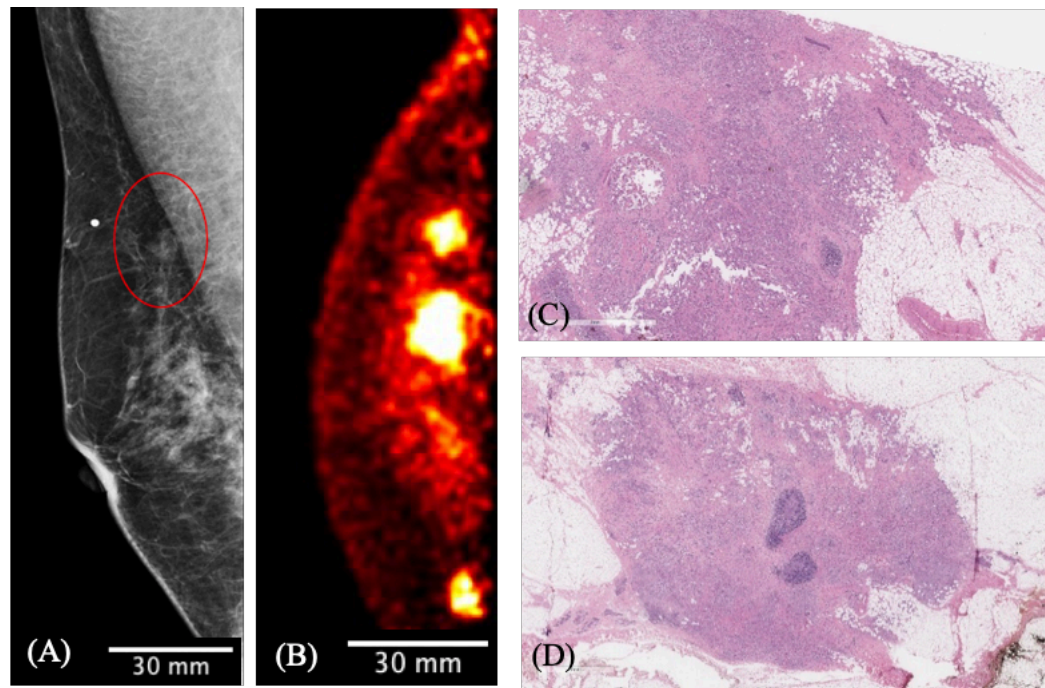


Figure 15. The MLO view digital mammography image (A) demonstrated the palpable mass (red circle) associated with the radiopaque marker placed on the patient's skin. The presented slice of Radialis PET camera CC image with 200 MBq injected  $^{18}\text{F}$ -FDG (B) identifies this lesion against the chest wall as well as two additional posterior masses; (C) view of largest focus showing invasive ductal carcinoma no special type, clip site reaction is present in the center of the tumor; (D) second invasive focus demonstrating similar morphologic features and histologic grade. The 3 regions of contrast enhancement identified by Radialis PET were all biopsy confirmed cancers.

Figure 16 presents MRI 3D maximum intensity projection images (Figure 16, A) acquired in a female patient showing multiple rounded and oval shape enhancing masses in both breasts. There is a noticeable discrepancy between MRI depicted lesions and the lack of focal uptake of  $^{18}\text{F}$ -FDG in the organ-targeted PET images acquired with a 37 MBq injection (Figure 16, B, C). This high-risk patient underwent programmed bilateral breast surgery (mastectomy) without malignancy identified in the surgical pathology report.

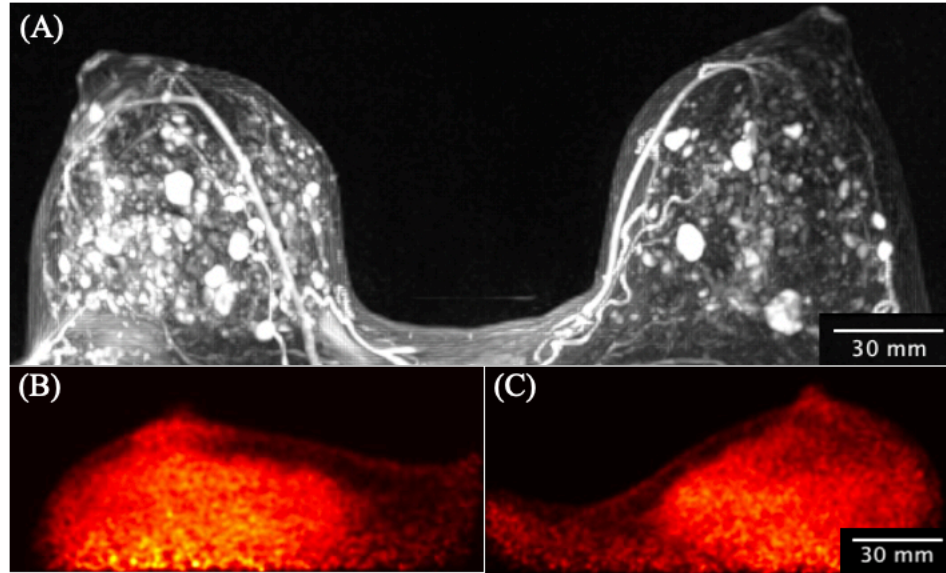


Figure 16. A 33 years-old high-risk female underwent pre-operative breast MRI with multiplicity of enhancing masses demonstrated by the 3D-MIP image (A) and without corresponding masses demonstrated by the Radialis PET camera images (B) with a 43 MBq injection. The mediolateral oblique views from the Radialis PET camera are presented for the left (B) and right (C) side without evident focal  $^{18}\text{F}$ -FDG uptake in either image. The surgical pathology results do not show signs of cancer.

The clinical WB PET images presented in Figure 17 (A, B) were acquired with a Siemens Biograph Vision WB PET/CT. Figure 17 (A) shows the full FOV slice with the region of the image with the breast expanded in (Figure 17, B) and the organ-targeted PET (Figure 17, C) of a 50-year-old female patient with a known malignancy in the right breast. 307 MBq of  $^{18}\text{F}$ -FDG was administered and the WB PET/CT image acquisition was performed after a 60-min uptake time. Immediately after the WB PET/CT examination, the patient was imaged with the Radialis organ-targeted PET camera. The WB PET/CT axial images identified an inhomogeneous hypermetabolic mass and a slightly hypermetabolic satellite nodule. Despite the shorter imaging time for the organ-targeted PET acquisition (5 min) the extent of the lesions is more clearly defined, both in terms of the extent of the lesions as well as the regions within the lesion with the highest functional activity. Smaller anatomical features such as the nipple are visible in the organ-targeted image while not being present in the WB images.

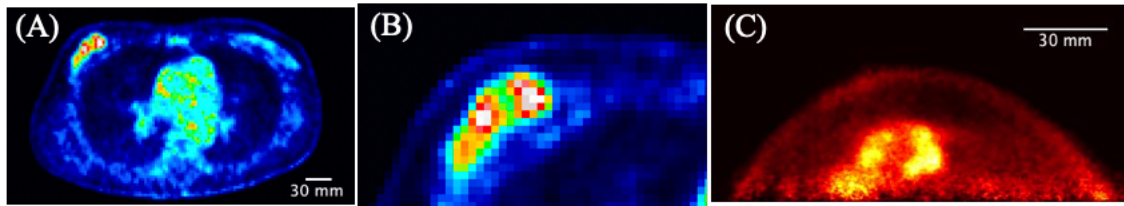


Figure 17. Side by side comparison of 307 MBq PET images from a breast cancer patient scanned with a Siemens Biograph PET/CT reconstructed using a time-of-flight reconstruction technique (TOF) (A and B) and with the Radialis PET system (C).

#### 4.4. Summary

The development of the organ-targeted PET technology described herein focused precisely on the matter of hardware-based improvements in sensitivity and count rate performance across a clinically useful activity range, down to low-dose activities at 1/10th of a standard dose [54]. The first clinical evaluation of the developed organ-targeted PET camera was devoted to breast cancer due to the clinical significance of high-sensitivity molecular breast imaging with  $^{18}\text{F}$ -FDG PET: it has the potential to overcome a well-known drawback of mammography that is low sensitivity in heterogeneous and extremely dense breasts [55] found in roughly 50% of the population [56]. Here, we demonstrate that the high-resolution and high-sensitivity of the Radialis organ-targeted PET permits effective visualization of breast lesions and can overcome the lesion obscurity (masking effect) experienced in mammography from dense breast tissue since  $^{18}\text{F}$ -FDG PET uptake is largely independent of tissue density. We also demonstrate a potential to address the high false-positive rate associated with gadolinium-enhanced breast MRI. The selected results from clinical trials demonstrate capability to image lesions at the chest wall, identify false-negative x-ray findings, and false-positive MRI findings, even at up to a 10-fold dose reduction in comparison with standard  $^{18}\text{F}$ -FDG doses (i.e., at 37 MBq or 1 mCi).

## **5. Evaluation of Quantitative Imaging Capabilities of a Clinical Organ-Targeted PET Camera**

The following section contains content submitted for publication in *Frontiers in Oncology*, entitled: Baldassi, B., Stiles, J., Bubon, O., Poladyan, H., Freitas, V., Komarov, B., Shahi, A., Maa-Hacquoil, H., Waterston, M., Aseyev, O., Reznik, A. “Image Quality Evaluation for a Clinical Organ-Targeted PET Camera.”

Baldassi is the first author.

This section presents the evaluation of quantitative imaging capabilities for the Radialis PET Camera conducted within the framework of clinical study in breast cancer patients. The contrast recovery capabilities in small structures are assessed with standardized and clinically relevant phantom measurements and results are compared with other commercial organ-targeted PET scanners. The scanner performance is demonstrated with quantitative lesion uptake assessment and 3-D visualization of abnormally metabolic tissues in breast cancer patients.

## 5.1. Abstract

A newly developed clinical organ-targeted PET system is tested with a set of standardized and custom tests previously used to evaluate the performance of Positron Emission Mammography (PEM) systems. Imaging characteristics related to standardized uptake value (SUV) and detectability of small lesions, namely spatial resolution, linearity, uniformity, and recovery coefficients, are evaluated.

In-plane spatial resolution was measured as 2.3 mm  $\pm$ 0.1 mm, spatial accuracy was 0.1 mm, and uniformity measured with flood field and NEMA NU-4 phantom was 11.7% and 8.3% respectively. Select clinical images are provided as reference to the imaging capabilities under different clinical conditions such as reduced  $^{18}\text{F}$ -FDG activity and time-delayed acquisitions. SUV measurements were performed for selected clinical images to demonstrate a capability for quantitative image assessment of different types of cancer including for invasive lobular carcinoma with comparatively low metabolic activity.

Quantitative imaging performance assessment with phantoms demonstrates improved contrast recovery and spill-over ratio for this PET technology when compared to other commercial organ-dedicated PET systems with similar spatial resolution. Recovery coefficients were measured to be 0.21 for the 1 mm hot rod and up to 0.89 for the 5 mm hot rod of NEMA NU-4 Image Quality phantom. Demonstrated ability to accurately reconstruct activity in tumors as small as 5 mm suggests that the Radialis PET technology may be well suited for emerging clinical applications such as image guided assessment of response to neoadjuvant systemic treatment (NST) in lesions smaller than 2 cm. Also, our results suggest that, while spatial resolution greatly influences the partial volume effect which degrades contrast recovery, optimized count rate performance and image reconstruction workflow may improve recovery coefficients for systems with comparable spatial resolution. We emphasize that recovery coefficient should be considered as a primary performance metric when a PET system is targeted for accurate lesion size and radiotracer uptake assessment.

## 5.2. Introduction

The diagnostic capabilities of organ-targeted PET systems relate to the ability to reconstruct the true activity within a lesion and depend on the conspicuity of small lesions at

different injected activities based on radiotracer uptake. The former is of particular importance in evaluating response to neoadjuvant systemic treatment (NST) in breast cancer patients - chemotherapy or hormonal therapy administered prior to surgical treatment [57]. Neoadjuvant treatment is increasingly being used to downstage and downsize the tumour and to facilitate breast conservation. Early and accurate assessment of the tumour's response to NST (i.e., the metabolic decline and the reduction in size) can help to use a personalized treatment regimen to achieve optimal response prior to surgery and to avoid the toxicity associated with ineffective treatments. A decline in tumour metabolism in response to NST can occur earlier than apparent changes in tumour size and anatomy (or may not correlate with anatomical changes at all [58]), thus making anatomical imaging modalities not well suited for the purpose of evaluating early treatment response. In contrast, PET molecular imaging with  $^{18}\text{F}$ -fluoro-2-deoxyglucose ( $^{18}\text{F}$ -FDG) may better reflect early treatment response through its ability to depict a decrease in tumour glucose metabolism that precedes a decrease in its anatomical size [59][60].

Recent trends to apply NST for tumours smaller than 2 cm in size [61] have put a stringent limit on PET/CT (Computed Tomography) performance in terms of quantitative assessment of the metabolic changes in tumours through measurements of standardized uptake value (SUV). In fact, when  $^{18}\text{F}$ -FDG uptake in small tumours is measured, the partial-volume effect (PVE), that is a consequence of finite spatial resolution, can lead to underestimation of activity concentrations in reconstructed PET images due to spill-over of counts between different regions within the image [62]. The PVE becomes significant for an imaging system where the dimensions of a tumour are less than two to three times the FWHM point spread function (PSF) of the system [63], as this can strongly influence the measured size and uptake of the lesion. Therefore, considering the lesser spatial resolution of most modern PET/CT scanners compared to targeted PET, PVE can affect SUV measurements and activity reconstruction in shrinking tumours that were around 2 cm prior to treatment. This may produce inaccuracies in assessing response to neoadjuvant treatment: a shrinking tumour will look larger but less aggressive due to signal spill-over from lesion-to-background caused by degradation of recovery coefficient. Alternatively, if NST results in partially necrotic centres within tumours, signal spill-in will falsely indicate a greater extent of viable tissue within the inactive parts of the tumour than in reality. The PVE is quantitatively assessed by the ratio between image-

derived and true activity measurements, commonly termed the recovery coefficient (RC), and depends on several factors which include the spatial resolution, count rate efficiency, and the reconstruction algorithm and parameters. [64]

The development of a high-sensitivity organ-targeted Positron Emission Tomography (PET) system – the “Radialis PET camera” – has spurred from the clinical need to reduce the radiation dose associated with functional (molecular) imaging while preserving the capability of small lesion detection inherent to organ-targeted PET [33, 65, 44, 66]. We have recently demonstrated that the Radialis PET camera has improved sensitivity, capable of significant dose reduction (factor of 10) in comparison to commercial whole-body (WB) PET scanners [66]. Standardized measurements were performed with NEMA NU-4 procedures adapted for the planar PET detector geometry, including spatial resolution, sensitivity, and system count rates. Selected clinical breast cancer images illustrate the system performance within a range of circumstances including varied radiation doses (37-370 MBq), presence of chest wall lesions, and lesion detectability in comparison to WB-PET, full field digital mammography (FFDM), and breast MRI. Increased sensitivity shown by NEMA NU-4 tests and high-efficiency radiotracer detection demonstrated with clinical images were achieved through development of a new type of modular detector architecture with four-side tileable sensor modules based on high-gain Silicon Photomultiplier (SiPMs) photosensors [26].

Standardized measurements within NEMA NU-4 are important to compare the Radialis PET camera to similar modalities, however these standards were developed without consideration of the latest hardware and software developments and therefore have faced recent criticism [67]. Indeed, the NEMA NU-4 requirement of back-projection image reconstruction does not represent the methods used in current real-world, clinical applications. Therefore, the described tests have potential flaws in accurately representing the system performance metrics during typical use. In addition, since NEMA NU-4 standard tests were developed for preclinical imaging, they do not account for unique aspects of clinical organ-targeted PET (e.g., relatively large field-of-view (FOV)) and detector architectures, including planar detectors and modular, adjustable gantry. Finally, the NEMA NU-4 phantom imaging conditions distinctly differ from clinical use and do not provide needed insights into true clinical capabilities and limitations.

A comprehensive assessment of imaging performance in organ-targeted PET requires additional tests that characterize imaging parameters not covered by NEMA NU-4 standard and which are more suitable for the intermediate FOV and modern iterative image reconstruction methods. Therefore, we follow the methodology developed and reported by others [44, 46, 68] to perform characterization of spatial resolution and linearity, flood field uniformity, and RC, with evaluation of NEMA NU-4 image quality phantom also included. The ability to recover the activity of small structures in the presence of background radioactivity is assessed using micro-spheres of different sizes in a hot background which mimic lesions in the body. The tests of RC, flood field uniformity, contrast to noise ratio (CNR) and the Rose Criterion [69] are of importance for assessing the ability of the system to apply SUV analysis to lesions of different size and for assessing uptake of a radiopharmaceutical.

Additionally, the modular design of our system may allow variability in the electronic functions between separate modules. These differences may cause spatial distortions along the FOV, as well as changes in uniformity between different modules. Thus, experiments with line sources (rather than point sources used in NEMA NU-4) and large-area flood phantoms can serve to better identify any discrepancies in spatial resolution, signal to noise ratio, and uniformity within the entire image space.

Finally, we present select clinical images with quantification of SUV and 3-D visualization of abnormally metabolic tissue. The measurements reported here provide a performance assessment of the Radialis PET camera, highlighting its capabilities for quantitative PET imaging.

For a variety of emerging clinical applications, the assessment of the size and activity uptake in a lesion is not less important than detection of the lesion itself. *While spatial resolution is one of the main specifications that is used to characterize PET system performance, high spatial resolution is required but not sufficient criterion for accurate contrast recovery.* We emphasize that systems with the same or comparable spatial resolution may report different recovery coefficients and different spill-over ratios. Here, we provide PET system performance metrics measured with standardized NEMA protocols, as well as adapted tests used by others [44, 46, 68] and discuss the differences in system performances with special emphasize on recovery coefficient in small lesions.

### **5.3. Materials and Methods**

The described Radialis organ-targeted PET Camera is used for all phantom and clinical imaging results presented here. The scanner acquires with the default clinical parameters and image reconstruction is performed with the default MLEM algorithm. Detector separation was configured to a minimal gap based upon the clinical case or phantom dimensions and ranged between 60 - 135 mm for the set of experiments. Reconstructed images are saved in DICOM format with 24 axial image slices in the XY plane. The image matrix is defined by a pixel size of 0.4 mm × 0.4 mm. The voxel dimension is determined by the detector separation divided into 24 equal components.

#### **5.3.1. Spatial Resolution and Linearity**

Measurement of spatial resolution was previously performed in accordance with pre-clinical NEMA standards. Here, spatial resolution is measured per WB PET standards by analyzing the line-spread function (LSF) of a line source of radioactivity in Figure 18 (top) [70, 71, 72]. A capillary tube, with a length of 44.4 cm and an inner diameter of 1.2 mm (which is approximately half of the anticipated spatial resolution), was filled with an <sup>18</sup>F-FDG solution. The line source was positioned halfway between the detectors axially and centrally in the y-axis, such that the source extends along the entire length of the x-axis FOV. Detected coincidence events are collected until at least 1 million events are recorded. The reconstructed image is analyzed by taking the LSF orthogonal to the line source axis. A gaussian fit is applied and the full width at half maximum (FWHM) for the LSF defines the spatial resolution quoted here [73]. LSF's were taken in 10 positions across the line source spanning the complete FOV. The average value of the FWHM was reported as the spatial resolution for the in-plane and cross-plane FOVs.

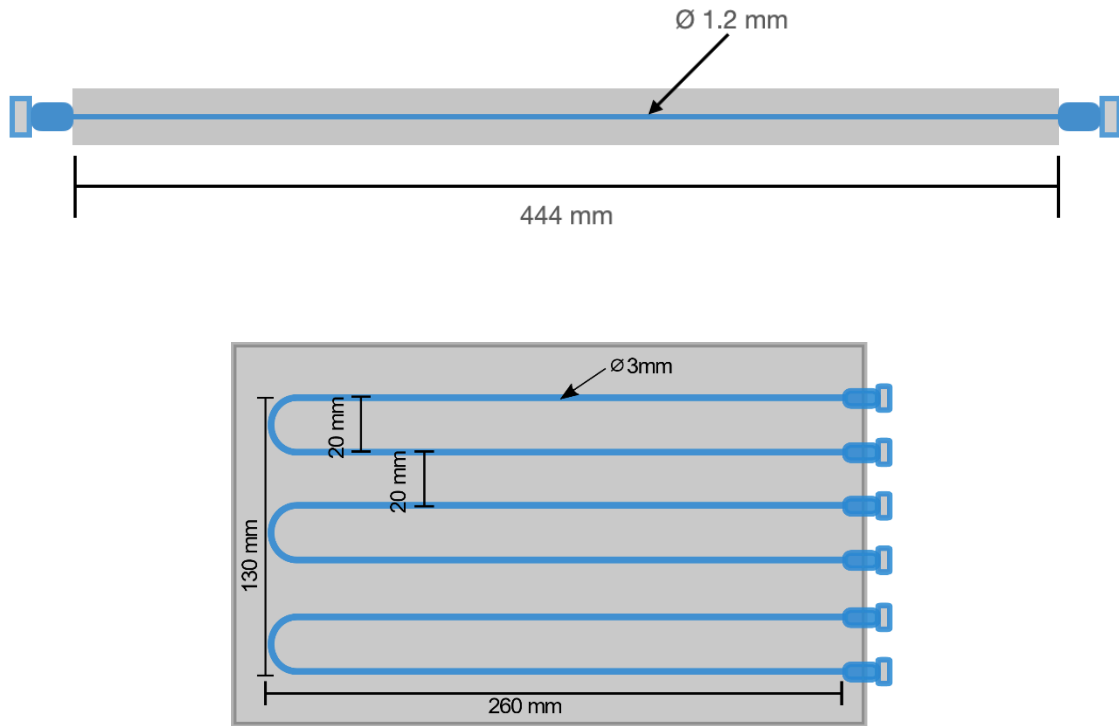


Figure 18. Schematic diagram of the fillable capillary phantom (top) and spatial linearity phantom (bottom) with markings for the line source separation and phantom dimensions.

Spatial linearity was measured with a linearity phantom shown in Figure 18 (bottom). Six capillary tubes were filled with  $^{18}\text{F}$ -FDG solution and arranged in a plastic jig to ensure parallel positioning with a center-to-center distance of 20 mm.

Image acquisition for the linearity phantom was performed in two different positions:

- 1) In the central XY plane ( $z = 0$  mm), with capillaries parallel to y-axis.
- 2) In the central XY plane ( $z = 0$  mm), with capillaries parallel to x-axis.

Measurements of spatial linearity are derived from pixel values perpendicular to the length of the capillary tubes. The peak pixel value location was determined for each parallel capillary and the separation between each peak was plotted. Variation in reconstructed peak position from known spacing is reported. The spatial accuracy of the reconstructed source is quantified as the difference in average reconstructed position from expected position. The acquisitions were performed at a detector separations of 90 mm-135 mm with the phantom centered between detectors.

### 5.3.2. Flood Field Uniformity

Measurement of flood field uniformity was performed using a flat phantom which is dimensionally greater than the FOV in order to assess imaging effects at the edge of the FOV [74,75]. The phantom was filled with 100  $\mu\text{Ci}$   $^{18}\text{F}$ -FDG activity and was positioned parallel to and equidistant from each detector. Image acquisition of at least 5 million coincidence events was performed with a detector separation of 80 mm. The image of the flood phantom was reconstructed with the default clinical parameters, using images from the first iteration and fifteenth iteration for analysis. A central ROI of 150 mm  $\times$  100 mm was chosen within which the statistical measurements were performed.

Measurements are reported for the mean, maximum, and minimum pixel value, and percentage standard deviation (%STD) as a measurement of noise. These values were calculated based on the methods described for determining the uniformity of the NEMA NU-4 small animal phantom [39] and are further explained below. The uniformity analysis was performed and used for per pixel efficiency corrections.

### 5.3.3. Recovery Coefficients

We compare RC under 4:1 and 10:1 lesion to background activity concentrations for PEM Flex Solo II [44] and MAMMI PET [46] commercial organ-dedicated PET scanners. Measurements were performed using micro-spheres of radioactivity placed between two 500 mL IV bags filled with background activity. The acquisition layout is presented in Figure 19. The spheres, with inner diameters of 4, 5, 6, and 8 mm, were each filled with the same activity concentration of  $^{18}\text{F}$ -FDG. The IV bags were also filled with  $^{18}\text{F}$ -FDG activity. Activity concentration of the background was 5 kBq/mL and 0.379 kBq/mL, with sphere activity concentrations of 20 kBq/mL and 3.79 kBq/mL, respectively. Image reconstruction was performed with the default clinical parameters. Detector separation was set to 90 mm to provide slight compression to the IV bags and to mimic clinical imaging conditions, where radioactive tissue is in contact with the detector surface. It should be noted that measurements for the PEM Flex Solo II scanner were performed with a similar experimental configuration as in Figure 19, with hot spheres of radioactivity sized from 8 mm to 30 mm between background activity at a 4:1 ratio [44]. Measurements

for the MAMMI PET were performed using a cylindrical phantom with hot cylinders in uniform background activity at a 10:1 ratio [46].

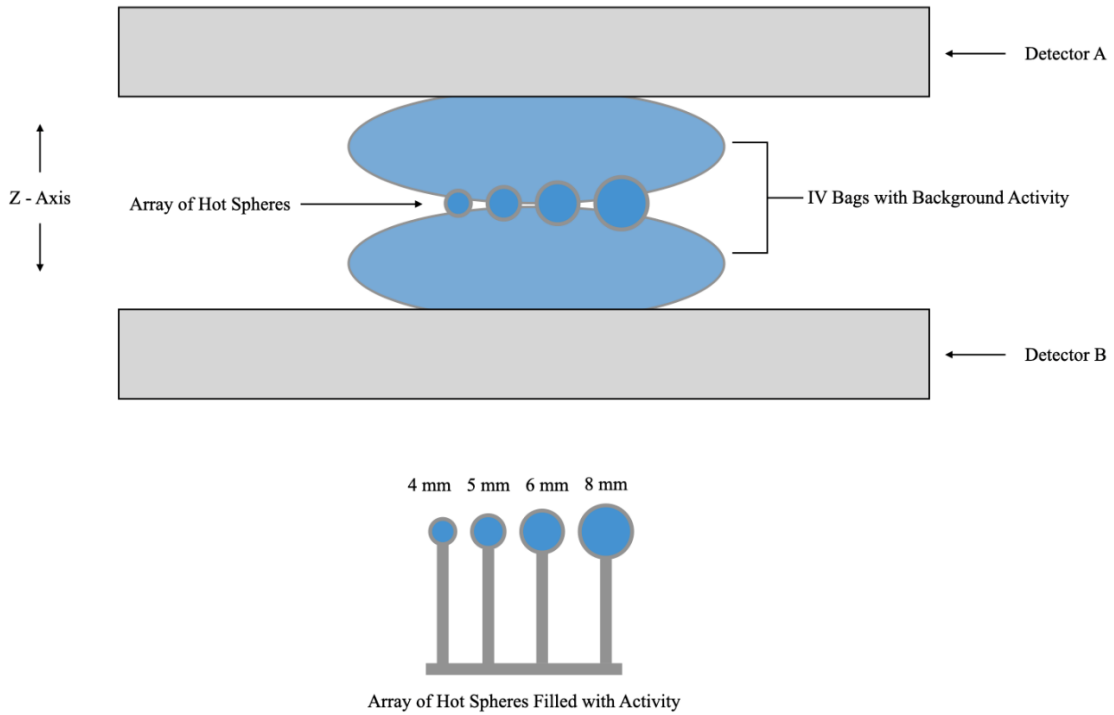


Figure 19. Schematic diagram of the acquisition layout for the recovery coefficient experiment showing hot spheres of radioactivity positioned between two IV bags for background activity and immobilized between detector heads. Note that the schematic is not to scale.

RCs for each micro-sphere were defined as relative and absolute measures. Relative RCs (Equation 12 and Equation 13) give the ratio between measured image values for hot-spheres and background IV bag regions, while absolute RCs (Equation 14) relate the measured activity concentration values to the true activity concentrations measured by a dose calibrator. Maximum image intensity values were measured within a circular region of interest (ROI) around each sphere and the mean image intensity values are calculated within a circular ROI proportional to the sphere diameter and in the uniform part of the IV bag for background. These values were recorded for each sphere in the image and plots were created for the recovery coefficients as a function of sphere diameter and activity concentration.

$$\text{relative } RC_{\text{mean}} = \frac{\text{mean (hot sphere ROI)}}{\text{mean (background)}} \quad \text{Equation 12}$$

$$\text{relative } RC_{\text{max}} = \frac{\text{maximum (hot sphere ROI)}}{\text{mean (background)}} \quad \text{Equation 13}$$

$$\text{absolute } RC_{\text{max}} = \frac{\text{maximum (activity concentration ROI)}}{\text{true (activity concentration ROI)}} \quad \text{Equation 14}$$

The percent contrast was also calculated for the hot micro-spheres positioned between two radioactive IV bags. The percent contrast in hot lesions ( $Q_H$ ) is calculated as follows:

$$Q_H = \frac{\frac{C_H}{C_B} - 1}{\frac{a_H}{a_B} - 1} \times 100 \quad \text{Equation 15}$$

Here,  $C_H$  and  $C_B$  represent mean activities in hot and background regions, respectively, while  $a_B$  and  $a_H$  represent true activities measured with a dose calibrator [46].

The contrast to noise ratio (CNR) was calculated based on the absolute difference between the mean counts in the hot spheres and the background (for the slice with the maximum hot sphere counts) and was normalized to the standard deviation of the background ( $SD_B$ , Equation 16). This value was used to determine the sphere detectability based on the Rose Criterion [69], which states that objects with  $CNR < 5$  are considered not detectable. Based on this, “pass” or “fail” values for detectability of each sphere in the three lesion-to-background ratio (LBR) acquisitions were reported.

$$CNR = \frac{|C_H - C_B|}{SD_B} \quad \text{Equation 16}$$

#### 5.3.4. Image Quality Phantom

NEMA NU 4 image quality phantom (Figure 20) contains hot and cold objects of different sizes allowing to complement and verify the measurements of RC as well as to

assess image uniformity and the spill-over ratio (SOR) in air and water for the default clinical reconstruction parameters. As shown in Figure 20, the phantom volume can be divided into two regions: a solid part with five fillable rods of different diameters to determine the activity recovery coefficients and to assess spatial resolution and partial volume effects of the scanner; and a fillable chamber with two hollow cylinders to be filled with nonradioactive water and air to determine the spill-over ratio in water and air, respectively. A uniform part of this fillable chamber is used for the uniformity and noise measurement, i.e., to determine the mean, maximum and minimum activity concentration and respective %STD similarly to section 5.3.2.

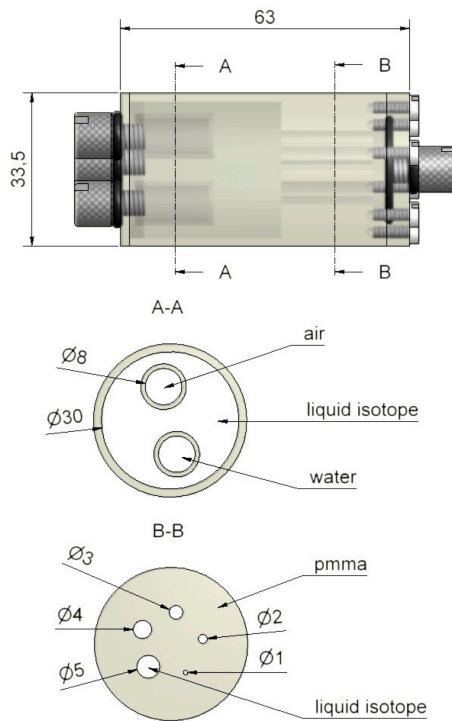


Figure 20. Design configuration and dimensions in mm of the NEMA NU-4 Image quality phantom. Source: [www.qrm.de/en/products/micro-pet-iq-phantom](http://www.qrm.de/en/products/micro-pet-iq-phantom)

The total activity within the phantom was 1.87 MBq. Acquisitions were performed with the phantom vertically oriented and at a detector separation of 110 mm to accommodate the mounting fixture. The acquisition was calibrated to acquire at least 10 million total events for accurate image reconstruction and processing. The image of the phantom was

reconstructed with the default clinical reconstruction parameters and therefore it also provides insight into the attenuation and scatter correction performance.

The uniformity measurement is performed in the central uniform region of the phantom and is based on a cylindrical volume of interest (VOI) with diameter of 22.5 mm and height of 10 mm. Values for the average activity concentration, maximum and minimum voxel values in VOI, and %STD are measured and reported.

The recovery coefficient measurement is performed on the five hot rods using a circular ROI with diameters twice the physical diameter of the rods. The pixel position with the maximum value in each ROI was identified, through which a transverse line profile was drawn. The mean pixel values measured for each profile are divided by the mean activity concentration measured in the uniformity calculation to determine the recovery coefficient for each hot rod in accord with NEMA protocols [39].

The standard deviation of the recovery coefficients per NEMA NU-4 is calculated as follows:

$$\%STD_{RC} = 100 \times \sqrt{\left(\frac{STD_{lineprofile}}{Mean_{lineprofile}}\right)^2 + \left(\frac{STD_{background}}{Mean_{background}}\right)^2} \quad \text{Equation 17}$$

A cylindrical VOI with diameter of 4 mm and height of 7.5 mm was selected in the central region of the cold (i.e., the air- and water-filled) chambers to assess the accuracy of the applied corrections. Indeed, although both chambers are nonradioactive, scattered annihilation photons and partial volume effect (PVE) due to finite spatial resolution may result in apparent activity in the cold chambers that is characterized by SOR values [76]. Explicitly, the SOR was defined as the ratio of the mean in each cold chamber to the mean of the hot uniform area.

The standard deviation of the SOR is calculated as follows:

$$\%STD_{SOR} = 100 \times \sqrt{\left(\frac{STD_{cold}}{Mean_{cold}}\right)^2 + \left(\frac{STD_{background}}{Mean_{background}}\right)^2} \quad \text{Equation 18}$$

Both RC and SOR are theoretically limited between 1 and 0.

### **5.3.5. Clinical Imaging Demonstration**

The clinical performance of the camera is demonstrated through image acquisition in breast cancer patients at varying injected doses of  $^{18}\text{F}$ -FDG within the framework of a clinical study at the Princess Margaret Cancer Centre of the University Health Network (UHN-PMCC) in Toronto, Canada [53]. Image reconstruction was performed using default clinical parameters. For selected images, segmentation and 3-D lesion volume analysis was performed using an open-source DICOM viewer (3D-Slicer, PET-IndiC).

## **5.4. Results**

### **5.4.1. Spatial Resolution and Linearity**

Reconstructed images of the capillary phantom were used for measurements of spatial resolution. The line cross-sectional profile at 10 different points, evenly distributed along the entire length of the phantom, was approximated by a Gaussian function, and the mean spatial resolution was measured from the average of individual FWHMs. The mean spatial resolution across the in-plane FOV is  $2.3 \pm 0.1$  mm, and the mean Z-axis resolution is  $7.9 \pm 0.7$  mm. The acquisitions were performed at different detector separations between 90 - 135 mm and the results were not dependent on the separation distance.

Spatial linearity measurements were performed on reconstructed images of the linearity phantom shown in Figure 18. The mean spatial accuracy in X and Y axes is found to be  $\pm 0.1$  mm. This performance is consistent across and at the edges of the FOV and the results were not dependent on the detector separation distance.

### **5.4.2. Flood Field Uniformity**

Image uniformity has been assessed in response to uniform exposure across the entire FOV with the flood field phantom. Reconstructed images of flood sources were analyzed for the first and 15<sup>th</sup> MLEM iteration and uniformity values are summarized in Table 9.

Table 9. Summary of pixel value uniformity results for the 1<sup>st</sup> and 15<sup>th</sup> MLEM reconstruction iterations.

Iterations	Mean	% STD	Min	Max
1	1515	4.1	1228	1717
15	1014	11.7	580	1769

For the 15<sup>th</sup> iteration used as a default reconstruction parameter, the reconstructed image of the flood field phantom has a uniformity across the FOV of 11.7% standard deviation from the mean value.

### 5.4.3. Recovery Coefficients

Reconstructed images of four micro-spheres placed between two 500 mL IV bags (used as uniform background) are shown in Figure 21 for lesion-to-background activity concentrations of 4:1 and 10:1. Corresponding point-spread functions across the hot spheres are used for calculation of the recovery coefficients from the measured maximum and mean values in each lesion and IV bag background. Recovery coefficients for different sphere sizes across all sphere-to-background ratios are summarized in Table 10 for comparison with PEM Flex Solo II.

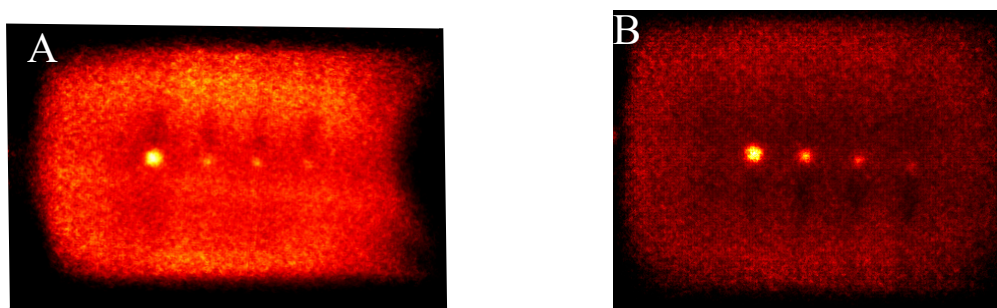


Figure 21. Reconstructed images showing the hot spheres and IV bags at sphere to background activity concentrations of 4:1 (A) and 10:1 (B). Note that visual non-uniformity in central regions of the bags is a result of the plastic hot-sphere fixture and a gap in activity at the physical interface between bags.

CNR for different sphere sizes across all sphere-to-background ratios are summarized in Table 11, along with assessment versus Rose's Criterion for confidence in assessment of image features [69]. These results suggest that sources 6 mm in diameter or

larger should receive an accurate contrast assignment for SUV measurement at various lesion-to-background ratios.

Table 10. Summarized recovery coefficients and percent contrast for Radialis PET and two other commercial organ-dedicated PET scanners from phantom experiments. Quoted spatial resolution values are provided for comparison.

Sphere Size	8.0 mm Radialis			4.0 mm Radialis			-	
	8.0 mm PEM Flex Solo II			4.5 mm MAMMI				
Activity Concentration	4:1			10:1			10:1	-
	8.4 mm MAMMI PET			PET				
Measured Quantity	RC Relative Mean	RC Relative Max	Absolute RC Max	RC Relative Mean	Percent Contrast (%)	RC Relative Mean	Percent Contrast (%)	Spatial Resolution (mm)
Radialis	2.45	3.27	0.82	4.93	44	2.73	20	2.3
PEM Flex Solo II	1.12	1.40	0.21	-	-	-	-	2.4
MAMMI PET	-	-	-	4.64	42	2.47	17	1.6

Table 11. Contrast to Noise ratio for each sphere size and sphere to background activity concentrations with corresponding Rose Criterion assessment.

Sphere Diameters	CNR for 10:1	Rose Criterion	CNR for 4:1	Rose Criterion
8 mm	22.7	PASS	12.8	PASS
6 mm	11.2	PASS	5.7	PASS
5 mm	5.1	PASS	2.8	FAIL
4 mm	2.2	FAIL	0.42	FAIL

#### 5.4.4. Image Quality Phantom

Transverse images acquired of the NEMA NU-4 Image Quality Phantom oriented along the Z axis are shown in Figure 22 with visible hot rods (A), uniform region (B), and

water and air reservoirs (C). Uniformity derived by measuring the standard deviation of the mean grey value in the uniform region of NEMA NU-4 image quality phantom is 8.31%. RC and SOR for the organ-targeted Radialis PET camera and PEM Flex Solo II organ-dedicated scanner are presented in Table 12 and show the expected trend towards full contrast recovery with increasing source sizes. The quoted spatial resolutions, all measured with the same standardized NEMA protocols, are provided to highlight the fact that systems with similar spatial resolution may recover contrast differently in small regions. The results were consistent across the range of detector separations tested (90 - 135 mm).

The smallest 1 mm rod in the NEMA NU-4 phantom, although difficult to visualize, has CNR of nearly 2 and shows 21% contrast recovery with a standard deviation of 16%. The largest rod, in comparison, has CNR of greater than 5 and a contrast recovery of 89%. The recovery coefficient as a function of sphere size follows a classical “S” shaped sigmoid curve [77].

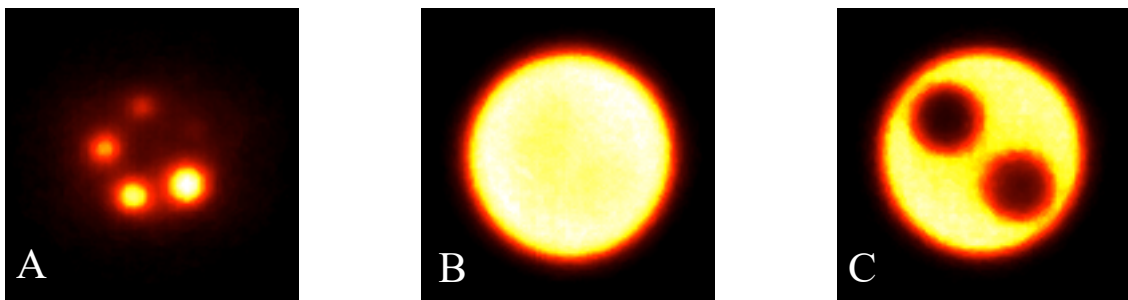


Figure 22. Reconstructed image slices for the NEMA NU-4 image quality phantom displaying the hot rods with diameters 1 - 5 mm for recovery coefficients (A), uniform region (B), and the air and water reservoirs (C).

Table 12. Summarized recovery coefficients, spill-over ratio and percent standard deviation for NEMA NU-4 phantom hot rods and cold cylinders for Radialis PET and another commercial organ-dedicated PET scanner [66,68]

Measured Quantity	RC (%STD)					SOR (%STD)		In-plane Spatial Resolution [mm]
	1 mm	2 mm	3 mm	4 mm	5 mm	Air Cylinder	Water Cylinder	
Region								-
Radials	0.21 (16)	0.31 (9)	0.53 (10)	0.73 (9)	0.89 (9)	0.30 (19)	0.20 (29)	2.3 ± 0.1
PEM Flex Solo II	0.1 (27)	0.12 (26)	0.22 (14)	0.38 (9)	0.45 (9)	0.64 (11)	0.52 (16)	2.4 ± 0.2

The larger SOR in air versus water was consistent across sets of measurements. Although it is not discussed in detail here, it was observed that the SOR is highly dependent on the LOR angular filtration. As it will be discussed below, reconstruction software optimization for clinical use requires careful consideration when the aim is to find optimal reconstruction parameters that yield accurate SOR and RC.

#### 5.4.5. Clinical Imaging

Clinical images are presented here to demonstrate cases where organ-targeted PET imaging is of significant clinical benefit in overcoming challenges in diagnosis, treatment planning, and monitoring response to a therapy.

Figure 23 shows a comparison among multimodality images for a multifocal cancer, specifically a FFDM CC view (Figure 23, A), Radialis organ-targeted PET CC view images (Figure 23, B, C), and an image of a 3-D reconstruction of multiple foci based on metabolic activity measured with Radialis PET (Figure 23, D). For the PET scan, 178 MBq of <sup>18</sup>F-FDG was administered to the patient and two subsequent imaging sessions (Figure 23, B, C) were acquired at 1 hour and 4 hours post-injection, with detector separation of 95 mm. The PET images demonstrate <sup>18</sup>F-FDG uptake in the extensive area that corresponds to the irregular mass detected on digital mammography, and

discrimination of multiple foci is still possible even though significant radiotracer decay has occurred. A reconstructed image of 3-D volume of abnormal tissue metabolism is derived from this data set and displayed in Figure 23 D.

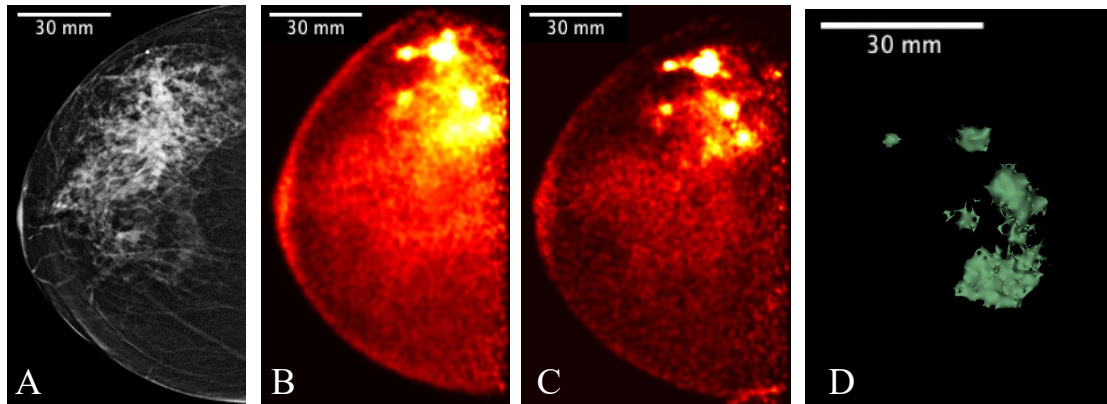
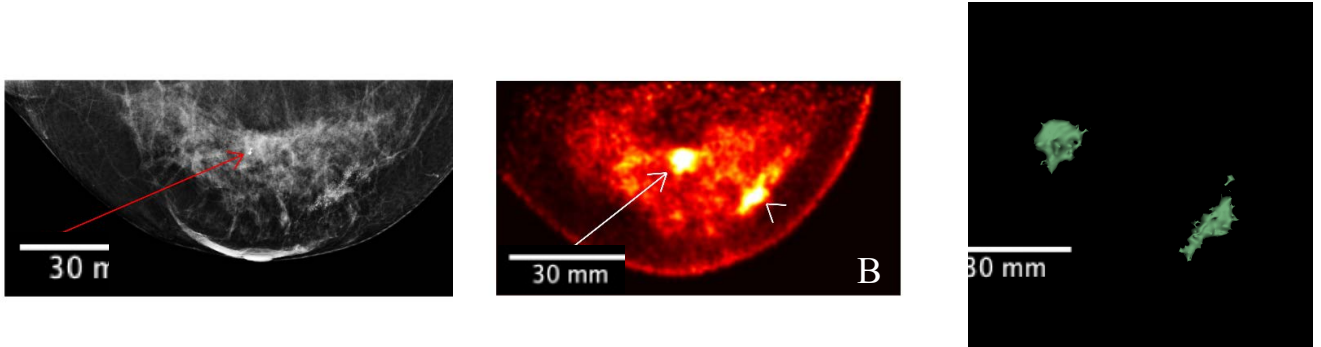


Figure 23. Images acquired for a 61-year-old female with right breast multifocal invasive and in situ ductal carcinoma. Images show the same breast in: A) FFDM in the CC plane with extensive distortion; B) 3-D Radialis PET image in the CC plane 1 hour after 178 MBq  $^{18}\text{F}$ -FDG injection; C) 3-D Radialis PET image in the CC plane where multiple distinct regions of contrast uptake are still evident 4 hours after  $^{18}\text{F}$ -FDG injection. Mean lesion SUV corrected for lean body mass ( $\text{SUV}_{\text{mean, LBM}}$ ) is 1.8, with  $\text{SUV}_{\text{max, LBM}}$  equal to 3.4.; (D) image of a 3-D volume of different foci generated from Radialis PET in the CC view based upon percentage of  $\text{SUV}_{\text{max}}$  tissue metabolism across all image slices.

In Figure 24, FFDM (Figure 24, A) is compared to Radialis organ-targeted PET image (Figure 24, B), and an image of a 3-D volume based on tissue metabolism measured with Radialis PET (Figure 24, C). A secondary cancerous site is visualized only in the PET image set (arrowhead in Figure 24, B). The patient was administered 37 MBq of  $^{18}\text{F}$ -FDG for image acquisition at 1-hour post-injection and images were acquired with detector separation of 120 mm. The images in Figure 23 and Figure 24 were segmented for analysis and a lean body-mass correction is applied to standardized uptake values quoted for lesions in both patients [78].



FFDM imaging (A) with red arrow indicating the site of a primary lesion. Radialis PET image (B) acquired 4 hr after injection with 37 MBq  $^{18}\text{F}$ -FDG and same craniocaudal (CC) view shows two distinct sites of contrast enhancement. The second site (arrowhead) is not detected in mammography. Both sites were confirmed cancerous by histopathology. 3-D volume (C) generated from the Radialis PET in the CC view based on a percentage of  $\text{SUV}_{\text{max}}$  tissue metabolism threshold across all image slices.  $\text{SUV}_{\text{mean, LBM}}$  for the primary lesion is 5.3, with  $\text{SUV}_{\text{max, LBM}}$  equal to 12.2.  $\text{SUV}_{\text{mean, LBM}}$  for the secondary lesion is 5.3, with  $\text{SUV}_{\text{max, LBM}}$  equal to 12.2.

Figure 25 displays two clinical cases of invasive lobular carcinoma (ILC) where distinct sites of enhancement are visible in the organ-targeted PET images and compared against x-ray images. In Figure 25 C, 188 MBq of  $^{18}\text{F}$ -FDG was administered to the patient and images were acquired 4 hours post-injection at a detector separation of 60 mm. In Figure 25 D, 191 MBq of  $^{18}\text{F}$ -FDG was administered to the patient and images were acquired 4 hours post-injection at a detector separation of 80 mm. The PET images demonstrate localized enhanced  $^{18}\text{F}$ -FDG uptake in each patient at the site of surgical pathology-confirmed ILC. The lean body-mass corrected standardized uptake value is reported for lesions in both patients.

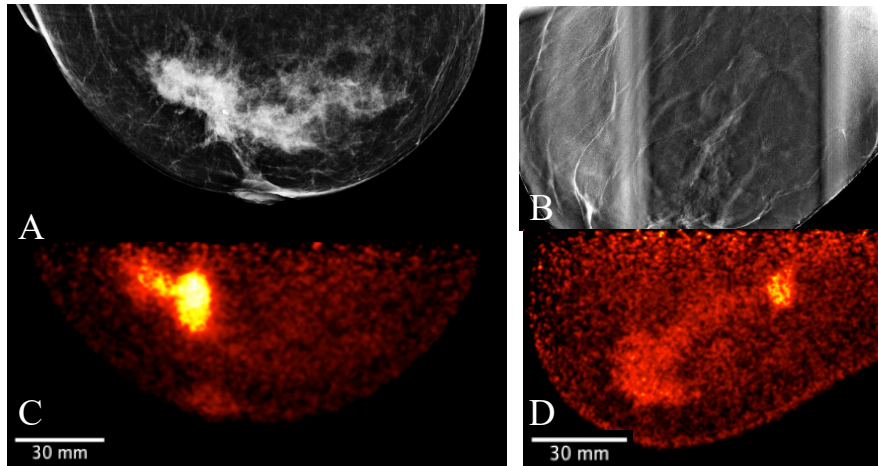


Figure 25. Clinical images acquired for two female patients with invasive lobular carcinoma who underwent x-ray mammography (A & B) and Radialis PET imaging 4-hours after radiotracer injection. The 50-year-old patient (A & C) received 188 MBq  $^{18}\text{F}$ -FDG injection and the image shows CC view mammography and PET images.  $\text{SUV}_{\text{mean, LBM}}$  for the lesion in (C) is 6.8, with  $\text{SUV}_{\text{max, LBM}}$  equal to 14.9. The 58-year-old patient (B & D) received 191 MBq  $^{18}\text{F}$ -FDG injection and the image shows a mammographic and Radialis PET mediolateral oblique (MLO) view.  $\text{SUV}_{\text{mean, LBM}}$  for the lesion in (D) is 2.2, with  $\text{SUV}_{\text{max, LBM}}$  equal to 4.4. Surgical pathology confirmed both lesions visible in the PET images as invasive lobular carcinoma.

## 5.5. Discussion

We report on selected performance indicators which are relevant to clinical use of organ-targeted PET, in particular for applications for monitoring response to NST. NST has become an integral part of breast cancer care for large cohorts of patients with locally advanced breast cancer and for those who may benefit from lesion size reduction before conservation surgery [59]. Assessing the degree of response to treatment is critically important and must be performed in a timely fashion to minimize the toxicity to patients not responding to treatment. PET imaging can assess tumour response as a result of treatment or disease progression in non-responsive patients and may track treatment effects in both breast and lymph nodes provided its imaging performance is adequate for quantitative assessment of changes in tumour size and metabolic activity.

Since small tumour size is a prognostic indicator for improved response to NST, it is increasingly applied for tumours  $< 2\text{cm}$  [79]. This places a stringent requirement on PET imaging to accurately reconstruct the true activity in small and downsizing lesions. Indeed, technological difficulties associated with non-zero spatial resolution and partial volume effects

lead to a reduced contrast assignment and blurred edges around activity boundaries in images. Because of the uncertainty in contrast assignment, small sources of radiation tend to smear out across the image, with a proportional reduction in observed contrast or activity. This affects the contrast recovery coefficients of the PET technology and reduces the ability to accurately assess SUV in small lesions in reconstructed images; the exact severity of this effect and clinical implications is discussed within the results presented here.

We place a special focus on evaluating the recovery coefficient as one of the major indicators of a PET system capabilities for quantitative assessment. Ideally, recovery coefficient is approaching unity for active lesions (most malignant tumours in PET) and zero for inactive lesions. However, the measured activity within an active lesion may appear as less than the actual value due to the PVE and RC. The inactive lesion will lead to the opposite result; an apparent increase or spill-in of activity to the cold region. Furthermore, smaller lesions will see more significant influence from the partial volume effect [<sup>80</sup>,<sup>81</sup>].

### **5.5.1. Spatial Resolution & Linearity**

Spatial resolution performance for the Radialis PET camera is comparable to commercially available organ-dedicated PET scanners [<sup>33</sup>,<sup>44</sup>,<sup>46</sup>,<sup>65</sup>]. Measurements presented here validate our previous point-source results of  $2.3 \pm 0.1$  mm in-plane and Z-axis resolution of  $7.9 \pm 0.7$  mm [<sup>66</sup>]. Since the line source has an inner diameter of 1.2 mm, this is not an intrinsic measurement of resolution, but rather a measurement of finite source size for comparison with whole-body PET. As the phantom extends beyond the full extent of the FOV, it was possible to confirm that the performance is not degraded at detector edges and that the FOV meets the dimensions of 230 mm by 173 mm.

Reconstructed images of the capillary and linearity phantom demonstrate accurate linear contrast assignment across the entire detector FOV. Intensity peaks from the activity distributions are reconstructed to  $\pm 0.1$  mm of the expected locations in images across both the X and Y axes thus showing excellent agreement between the expected and measured source locations. Since the linearity phantom extends beyond the FOV, measurements performed to the full extent of the FOV ensures no image distortion at any position within the FOV or at detector edges. Equivalent results are achieved at all four

edges of the FOV by reorienting the phantom for measurements, and these findings are consistent with those previously reported for point-source acquisitions [66].

### **5.5.2. Image Uniformity**

The uniformity in both tested phantoms (i.e., flood field phantom and NEMA NU-4 Image Quality phantom) degrade as a result of increasing MLEM iterations, an expected outcome due to the nature of iterative maximum likelihood reconstruction algorithms [82]. Compared to flood field uniformity, the small animal phantom has a measured standard deviation similar to values reported for pre-clinical PET scanners and PEM systems [44, 83]. The reconstructed small animal phantom image also demonstrates the ability to visualize the small rods of radioactivity, with the 1mm rod discernible by intensity profiles.

Indeed, it is well known that the expectation-maximization algorithm enhances noise and may contribute to distortions near edges with increasing iterations. Assessment of phantom and clinical image data to optimize detection of small details has resulted in the use of 15 iterations as a default setting for the organ-targeted PET scanner's clinical image reconstruction. Image non-uniformity is subsequently reduced by applying optimized MRP filtration within the reconstruction workflow.

### **5.5.3. Recovery Coefficients**

Table 10 summarizes the recovery coefficient and percent contrast values for the Radialis PET camera and for two other organ-dedicated PET scanners, namely PEM Flex Solo II and MAMMI PET. Quantitative comparison with PEM Flex Solo II was performed at the reported 4:1 activity concentration [44]. Despite comparable spatial resolution and detector geometry, all RC values are more than two times better for Radialis PET versus PEM Flex Solo II. In comparison with another organ-dedicated PET scanner, MAMMI PET, which reports nearly 50% higher spatial resolution than Radialis PET (1.6 mm vs. 2.3 mm), the Radialis PET camera has similar yet slightly improved contrast recovery at 10:1 activity concentration, which was the only reported value by MAMMI PET [46]. We believe that the improved contrast recovery is a result of greater count efficiency and optimized image reconstruction workflow [66]. This claim is subject to further investigation

in order to quantify the extent by which count statistics and image reconstruction affect contrast recovery.

The current approach to evaluate PET system performance in terms of confident detectability of small lesions is based on Rose criterion which requires  $CNR > 5$  [69]. For 4:1 activity concentration, the Radialis PET camera passes Rose criterion for spheres sized 6 mm and larger. This agrees with theoretical guidelines commonly used in WB PET where the minimum size of spheres that can be measured without underestimation in size and activity is 2.7 times the FWHM spatial resolution of the system [77]. However, for 10:1 activity concentration, the Radialis PET camera passes the Rose criterion for spheres smaller than 2.7 times the FWHM (5 mm or 2.17 times the FWHM of 2.3 mm). This indicates that, although theoretical guidelines are largely applicable in WB PET with comparatively low spatial resolution, the ability to reconstruct true activity in high spatial resolution organ-dedicated PET stem from increased count statistics and an ability to apply more rigorous corrections and filtration. Although we do not want to downplay the importance of high spatial resolution in molecular imaging, our results suggest that a system's contrast recovery capability should be assessed as a significant performance indicator when quantitative assessment of tumour uptake is needed [84].

#### **5.5.4. Image Quality Phantom**

While the suitability of the NEMA NU-4 Image Quality phantom for clinical PET systems is contested in the literature [41], we used it to compare the Radialis PET camera to a commercially available organ-targeted scanner with similar spatial resolution and planar detector architecture, the PEM Flex Solo II. Both scanners visualized hot rods similarly in the NEMA NU-4 phantom, but Radialis PET demonstrated improved RC for 1-5 mm hot rods and lower SOR for air and water-filled cylinders. This suggests that underestimation of reconstructed activity compared to actual activity is not solely due to limited spatial resolution. It also calls into question the universality of a commonly used criterion for the accuracy of reconstructed activity, which links partial volume effect to 2.7-3 times the FWHM of spatial resolution [77,85,86] without consideration of other scanner parameters.

Further investigation is needed, but it seems plausible that the higher RC and lower SOR achieved with the Radialis organ-targeted PET system can be attributed to an optimized image reconstruction workflow, a larger field of view, and higher count rate performance. These factors improve the statistical accuracy of measurements, reduce noise, and allow for more rigorous filtration of scattered radiation and random coincidences.

### 5.5.5. Clinical Images

The clinical images presented in this study showcase the potential of organ-targeted PET in breast cancer clinical practice. The results highlight the ability of organ-targeted PET to not only visualize the spatial distribution of abnormally metabolic tissue but to also quantify its properties in terms of SUV and reconstruct tumor volume based on metabolic activity.

Figure 23 presents a comparison between FFDM and two Radialis PET images acquired at 1-hour and 4-hours post  $^{18}\text{F}$ -FDG injection. Despite the changes in image contrast as activity decays post-injection, the radiologist's visual assessment of multifocal cancers remained unaffected. The multiple regions of enhanced  $^{18}\text{F}$ -FDG uptake (indicative of multifocal cancers) remained conspicuous even 3 hours after the initial scan and 4 hours from the time of radiotracer administration. Additionally, the 3-D metabolic volume generated from the latter image provides a unique visualization of abnormally metabolic tissue, allowing quantitative tracking of changes in mass volume of abnormally metabolic tissue above a certain threshold.

Lesion SUVs for the clinical images presented in Figure 23 to Figure 25 are quoted in Table 13, with lean body mass (LBM) correction applied to account for potential overestimation of glucose uptake in obese patients [87]. For images in Figure 23, Mean  $\text{SUV}_{\text{LBM}}$  and Maximum  $\text{SUV}_{\text{LBM}}$  significantly increase in the course of time after the injection (1.4 vs. 2.2  $\text{SUV}_{\text{LBM, mean}}$ , and 3.5 vs. 8.0  $\text{SUV}_{\text{LBM, max}}$ , Table 13) [88], which is a result of different wash-out mechanisms for cancerous and benign tissues [89]. Since  $\text{SUV}_{\text{max}}$  is a significant predictor of tumor detectability, these findings suggest that the scanning protocol may be optimized by increasing the time interval between injection and scanning. The Radialis PET camera is highly sensitive and has improved true coincidence

detection. This results in a high signal-to-noise ratio, and if the uptake period is longer, the activity decay may not negatively impact image contrast. This enables larger SUV values which may improve the accuracy of tumor assessments.

Table 13. Lean body mass corrected standardized uptake values for breast lesions in Figures 21-23.

Patient		Mean SUV <sub>LBM</sub> (g/mL)	Maximum SUV <sub>LBM</sub> (g/mL)	Elapsed Time Post- Injection (hours)
Figure 23	Primary lesion	1.4	3.5	1
	Primary lesion	2.2	8.0	4
Figure 24	Primary lesion	5.3	12.2	1
	Secondary lesion	5.3	10.7	1
Figure 25	Patient A	6.8	14.9	4
	Patient B	2.2	4.4	4

Figure 24 shows fundamental advantages of organ-targeted PET in comparison to mammography images for the purpose of both lesion detection and ability for treatment follow-up. The organ-targeted PET image (B) with 37 MBq <sup>18</sup>F-FDG injection shows two distinct sites of histopathology-confirmed cancerous contrast enhancement, the second of which (arrowhead, Figure 24, B) is not detected in mammography, even in retrospect. This illustrates the high specificity and sensitivity of Radialis PET imaging in detecting lesions in radiologically dense breast tissue, even at low doses of radiotracer. The measurement of SUV in both the primary and secondary lesions is performed under conditions of ten-times reduced dose, compared to the standard dose of 370 MBq used in PET diagnostic procedures [90].

Figure 25 illustrates the detection and quantification of invasive lobular carcinoma (ILC) with Radialis organ-targeted PET. ILC is the second most common type of invasive breast cancer, affecting approximately 1 in 10 patients, and its unique biological characteristics make it challenging to detect compared to invasive ductal carcinoma (IDC), the most common type of breast cancer [91,92]. ILC typically exhibits lower FDG uptake

compared to IDC [93]. This is further compounded by the fact that ILC often presents as diffuse disease with a lack of a clear border, making it more challenging to visualize on PET images. Despite these challenges, Radialis organ-targeted PET images have shown clear enhancement at the sites of surgical pathology-confirmed ILC. Also, the  $SUV_{max}$  correlates well with the lesion size and the findings are consistent with expected results, as FDG uptake may be considered predictive of disease aggressiveness and prognosis for patients with ILC [94,95,96]. We believe that this is due to the overall high sensitivity of Radialis PET and an optimized scanning protocol, which includes a 4-hour time period between injection and scanning. Since various NST's are applied depending on ILC subtype, with a growing trend toward long-course treatments, organ-targeted PET follow-ups may be of particular utility for accurate staging and treatment adjustments [92].

## 5.6. Conclusion

The set of measurements performed has revealed a specific peculiarity in high-resolution organ-dedicated PET. We find that the ability to detect and accurately reconstruct true activity in small objects is highly dependent on a broad set of parameters which define PET system performance, and that high spatial resolution alone does not guarantee accurate contrast recovery in small objects. Organ-targeted devices are already understood to exhibit higher spatial resolution than WB PET. Without being tied to other parameters, spatial resolution is not the only metric which defines the clinical utility of a PET system, especially in the context of quantitative measurement of response to therapy.

Organ-targeted PET is positioned to significantly impact the area of neoadjuvant systematic therapy. NST is rapidly evolving as a major trend in breast cancer care [57], but its use in treatment without a tool for evaluating its efficacy rises a concern about its widespread applications [86]. Quantitative organ-targeted PET has all the potential to become an integral part of individual and comprehensive treatment evaluation and early identification of non-responders [63,97]. Since NST is increasingly applied to patients with early-stage breast cancer, we expect a requirement to image and reconstruct activity in small lesions with low uptake (although the clinical validity of organ-targeted PET for NST must be evaluated in prospective clinical trials). Nevertheless, our result suggest that recovery coefficient shall be considered as a significant performance metric for PET systems targeted for small lesion detection, size

assessment, and activity uptake quantification. While factors influencing contrast recovery at the lower limits of detection must still be evaluated, the research indicates that solely chasing improvements in spatial resolution may not be cost-efficient. In addition, optimizing the scanning protocol may be a promising strategy for enhancing the performance and diagnostic value of PET imaging.

Overall, quantitative organ-targeted PET has the potential to open new frontiers in PET clinical utility for evaluating early NST response, optimizing its regimen to achieve the maximum pathological effect or identification of non-responders to continuously improve patient outcomes, especially given the emergence of new NAC options and new drugs being constantly developed.

## 6. Thesis Summary and Conclusions

### 6.1. Concluding Remarks

Organ-targeted PET is a medical imaging modality which is uniquely suited to address multiple unmet needs in current and emerging clinical applications. The organ-targeted PET technology developed and described here has demonstrated an improved ability to accurately quantify radiotracer uptake and clinical capabilities for breast imaging with less than 70 MBq radiotracer dose. Along with detector hardware improvements, which include scintillator material and photosensor characteristics, the main element that influences PET detection sensitivity is scanner geometry. Here, we show that the sensitivity in organ-targeted PET can be significantly improved with high-performing PET sensors arranged in a planar geometry and with sufficient FOV to provide increased solid angle coverage to maximize radiotracer signal collection. The optimization of the planar FOV was achieved using a seamless block detector array combined with high-yield scintillation crystals, high-gain solid-state photodetectors, adjustable detector temperature control, and acquisition electronics specially designed for organ-targeted PET.

Clinical trials with  $^{18}\text{F}$ -FDG PET in breast imaging revealed that this technology is well-suited for identifying a variety of cancers, even at a 10-fold dose reduction in comparison with standard WB PET, and is capable of showing clinical detail which is not visible using commercial WB PET scanners. This ability suggests that organ-targeted PET may be particularly well-suited to assessing tumour metabolic response during treatment and in applications with emerging targeted radiotracers. This research indicates that the recovery coefficient is a definitive performance metric for PET systems targeting small lesion detection, size assessment, and activity uptake quantification. Ongoing study will look to establish the complete set of factors which influence a system's contrast recovery at the lower limits of detection.

Overall, this Thesis demonstrates the significant advancement in organ-targeted PET technology through maximizing PET detection sensitivity and accurately reconstructing uptake of a radiopharmaceutical in small structures. The significance of this breakthrough lies in its immense potential to push the boundaries of early disease diagnosis and treatment

assessment across a diverse spectrum of medical conditions which include cancer, cardiovascular disease, and neurological disorders.

## 7. References

- 
- <sup>1</sup> Wadsak, W., and M. Mitterhauser. Basics and principles of radiopharmaceuticals for PET/CT. *Eur. J. Radiol.* 73.3 (2010): 461-469.
- <sup>2</sup> Shahhosseini, Soraya. PET Radiopharmaceuticals. *IJPR* vol. 10,1 (2011): 1-2.
- <sup>3</sup> Conti, Maurizio, and Lars Eriksson. Physics of pure and non-pure positron emitters for PET: a review and a discussion. *EJNMMI physics* 3 (2016): 1-17.
- <sup>4</sup> Belov, Vasily V., et al. Iodine-124 as a label for pharmacological PET imaging. *Mol. Pharm.* 8.3 (2011): 736-747.
- <sup>5</sup> Madsen, M. T. Recent advances in SPECT imaging. *J. Nucl. Med.*, (2007). 48(4), 661-673.
- <sup>6</sup> Renker, D., 2004, Photosensors. *Nuclear Instruments and Methods in Physics Research A* 527, 15-20.
- <sup>7</sup> Humm, J. I., Rosenfeld A., Del Guerra, A. From PET detectors to PET scanners. *EJNMMI* (2007) 30, 1574-1597
- <sup>8</sup> Shao, Y., et. al. Design studies of a high-resolution PET detector using APD arrays. *IEEE Trans Nucl Sci*, (2000). 47(3 PART 3), 10511057. <https://doi.org/10.1109/23.856546>
- <sup>9</sup> Lecoq, P., Valera, J. Clear-PEM, a Dedicated PET Camera for Mammography. *Nucl. Instrum. Methods Phys. Res.* (2002). A 486, 1-6.
- <sup>10</sup> S. Cova, et. al., Avalanche photodiodes and quenching circuits for single photon detection. *Appl. Opt.* (1996), vol. 35, no. 12, pp. 1956–1976,
- <sup>11</sup> Gundacker, S., & Heering, A. The silicon photomultiplier: fundamentals and applications of a modern solid-state photon detector. *Phys. Med. Bio.* (2020) 65(17), 17TR01.
- <sup>12</sup> Subramaniam, R. M. Precision Medicine and PET/Computed Tomography: Challenges and Implementation. *PET Clin.* (2017). 12(1):1-5.
- <sup>13</sup> Miles, K. A., Voo, S. A., Groves, A. M. Additional Clinical Value for PET/MRI in Oncology: Moving Beyond Simple Diagnosis. *J. Nucl. Med.* (2018), 59 (7) 1028-1032
- <sup>14</sup> Subramaniam, R. M. Nuclear Medicine and Molecular Imaging—An Impactful Decade of Contributions to Patient Care and Driving Precision Medicine. *Am. J. Roentgenol.* (2017). 209:2, 241-242

- 
- <sup>15</sup> Wang, X., Zhong, X., Cheng, L. Titanium-based nanomaterials for cancer theranostics. *Coord. Chem. Rev.* (2021) 1;430:213662.
- <sup>16</sup> Miyake, K.K., Nakamoto, Y. & Togashi, K. Current Status of Dedicated Breast PET Imaging. *Curr Radiol Rep.* (2016) 4, 16 <https://doi.org/10.1007/s40134-016-0145-0>
- <sup>17</sup> Narayanan, D., and Berg, W.A. Use of Breast-Specific PET Scanners and Comparison with MR Imaging. *Magn. Reson. Imaging Clin.* (2018). vol.26,2, 265-272. doi:10.1016/j.mric.2017.12.006
- <sup>18</sup> Hathi, D. K. et al. Evaluation of primary breast cancers using dedicated breast PET and whole-body PET. *Sci. Rep.* (2020). 10, 21930
- <sup>19</sup> Moliner, L., Rodríguez-Alvarez, M.J., Catret, J.V. et al. NEMA Performance Evaluation of CareMiBrain dedicated brain PET and Comparison with the whole-body and dedicated brain PET systems. *Sci Rep.* (2019) 9, 15484. <https://doi.org/10.1038/s41598-019-51898-z>
- <sup>20</sup> Nakamoto R., et al. Diagnostic performance of a novel dedicated breast PET scanner with C-shaped ring detectors. *Nucl Med Commun.* (2017). 38(5):388-395. doi: 10.1097/MNM.0000000000000661. PMID: 28306620.
- <sup>21</sup> García H. T., et al. Performance evaluation of a high resolution dedicated breast PET scanner. *Med Phys.* (2016). 43(5):2261. doi: 10.1118/1.4945271. PMID: 27147338.
- <sup>22</sup> Phunpueok, A., Chewpraditkul, W., Limsuwan, P., Wanarak, C., Light output and energy resolution of Lu<sub>0.7</sub>Y<sub>0.3</sub>AlO<sub>3</sub>:Ce and Lu<sub>1.95</sub>Y<sub>0.05</sub>SiO<sub>5</sub>:Ce scintillators. *Procedia Eng.* (2012). 32, 564–570.
- <sup>23</sup> Gierlik, Michał, et al. Comparative study of large NaI (Tl) and BGO scintillators for the EUROpean Illicit TRAfficking Countermeasures Kit project. *IEEE Trans Nucl Sci* 53.3 (2006): 1737-1743.
- <sup>24</sup> Mouhti, I., et al. Characterization of CsI (Tl) and LYSO (Ce) scintillator detectors by measurements and Monte Carlo simulations. *Appl Radiat Isot.* 154 (2019): 108878.
- <sup>25</sup> Browne, E., Junde, H. Nuclear data sheets for A=176. *Nucl. Data Sheets* 84, 337–486 (2002).
- <sup>26</sup> Reznik, Alla; Bubon, Oleksandr; Teymurazyan, A. Tileable block detectors for seamless block detector arrays in Positron Emission Mammography. (2017). Patent WO2017/143442A1. World Intellectual Property Org.

- 
- <sup>27</sup> Anger, H. O. Scintillation Camera With Multichannel Collimators. Uclrl-11387. UCRL [reports]. *U.S. At. Energy Comm.* (1964). 31, 70–86
- <sup>28</sup> Alenius, S. & Ruotsalainen, U. Bayesian image reconstruction for emission tomography based on median root prior. *Eur. J. Nucl. Med.* (1997). **24**, 258–265
- <sup>29</sup> Huang, B., Law, M. W.-M., & Khong, P.-L. Whole-Body PET/CT Scanning: Estimation of Radiation Dose and Cancer Risk. *Radiology*, (2009). 251(1), 166–174.  
doi:10.1148/radiol.2511081300
- <sup>30</sup> Hruska C. B. & O'Connor M. K. Curies, and Grays, and Sieverts, Oh My: A Guide for Discussing Radiation Dose and Risk of Molecular Breast Imaging. *J Am Coll Radiol.* (2015). 12(10):1103-1105. Doi:10.1016/j.jacr.2015.07.001
- <sup>31</sup> Rehani M.M. & Brady Z. Contemporary issues in radiation protection in medical imaging: introductory editorial. *Br J Radiol.* (2021) Oct;94(1126):bjr20219004. doi: 10.1259/bjr.20219004. PMID: 34545765.
- <sup>32</sup> Weber, W. A. et al. The Future of Nuclear Medicine, Molecular Imaging, and Theranostics. *J. Nucl. Med.* (2020). 61, 263S-272S
- <sup>33</sup> Gonzalez, A. J., Sanchez, F. & Benlloch, J. M. Organ-Dedicated Molecular Imaging Systems. *IEEE Trans. Radiat. Plasma Med. Sci.* (2018). 2, 388–403
- <sup>34</sup> Hendrick, R. E. Radiation doses and cancer risks from breast imaging studies. *Radiology* (2010). 257, 246–253
- <sup>35</sup> Catana, C. The Dawn of a New Era in Low-Dose PET Imaging. *Radiology* (2019). 290, 657–658
- <sup>36</sup> O'Connor, M. K. et al. Comparison of radiation exposure and associated radiation-induced cancer risks from mammography and molecular imaging of the breast. *Med. Phys.* (2010). 37, 6187–6198
- <sup>37</sup> Poladyan, H., Bubon, O., Teymurazyan, A., Senchurov, S. & Reznik, A. Gaussian position-weighted center of gravity algorithm for multiplexed readout. *Phys. Med. Biol.* (2020). 65.
- <sup>38</sup> Poladyan, H., Bubon, O., Teymurazyan, A., Senchurov, S. & Reznik, A. Gain invariant coordinate reconstruction for SiPM-Based pixelated gamma detectors with multiplexed readout. *IEEE Trans. Instrum. Meas.* (2020). 69, 4281–4291

- 
- <sup>39</sup> NEMA NU 4-2008. Performance measurements of Small Animal Positron Emission Tomographs. (2008). National Electrical Manufacturer's Association
- <sup>40</sup> Daube-Witherspoon, M. E. & Muehllehner, G. Treatment of axial data in three-dimensional PET. *J. Nucl. Med.* (1987). 28, 1717–1724
- <sup>41</sup> Hallen, P., Schug, D. & Schulz, V. Comments on the NEMA NU 4-2008 Standard on Performance Measurement of Small Animal Positron Emission Tomographs. *EJNMMI Phys.* (2020). 7
- <sup>42</sup> Schneider, C. A., Rasband, W. S. & Eliceiri, K. W. NIH Image to ImageJ: 25 years of image analysis. *Nat. Methods.* (2012). 9, 671–675
- <sup>43</sup> Weissler, B. et al. MR compatibility aspects of a silicon photomultiplier-based PET/RF insert with integrated digitisation. *Phys. Med. Biol.* (2014). 59, 5119–5139
- <sup>44</sup> MacDonald, L. et al. Clinical Imaging Characteristics of the Positron Emission Mammography Camera: PEM Flex Solo II. *J. Nucl. Med.* (2009). 50, 1666–1675
- <sup>45</sup> Smith, M. F., Majewski, S. & Raylman, R. R. Positron Emission Mammography with Multiple Angle Acquisition. *IEEE Nucl. Sci. Symp. Med. Imaging Conf.* (2002). 3, 1892–1896
- <sup>46</sup> Moliner, L. et al. Design and evaluation of the MAMMI dedicated breast PET. *Med. Phys.* (2012). 39, 5393–5404
- <sup>47</sup> Soriano, A. et al. Performance evaluation of the dual ring MAMMI breast PET. *IEEE Nucl. Sci. Symp. Conf. Rec.* (2013). 13–16
- <sup>48</sup> Teixeira, S. C. et al. Evaluation of a hanging-breast PET system for primary tumor visualization in patients with stage I-III breast cancer: Comparison with standard PET/CT. *Am. J. Roentgenol.* (2016). 206, 1307–1314
- <sup>49</sup> Van Sluis, J. et al. Performance characteristics of the digital biograph vision PET/CT system. *J. Nucl. Med.* (2019). 60, 1031–1036
- <sup>50</sup> Miller, M. A. Focusing on high performance. Advanced Molecular Imaging: Vereos PET/CT. *Product Content White Paper*, Philips Medical. (2016).
- <sup>51</sup> Vandenberghe, S., Moskal, P. & Karp, J. S. State of the art in total body PET. *EJNMMI Phys.* (2020). 7

- 
- <sup>52</sup> Xing, Y., Qiao, W., Wang, T. et al. Deep learning-assisted PET imaging achieves fast scan/low-dose examination. *EJNMMI Phys.* (2022). 9, 7 <https://doi.org/10.1186/s40658-022-00431-9>
- <sup>53</sup> Evaluating Positron Emission Mammography Imaging of Suspicious Breast Abnormalities. Clinical Trial. Identifier: NCT03520218
- <sup>54</sup> Schaefferkoetter J, Nai YH, Reilhac A, Townsend DW, Eriksson L, Conti M. Low dose positron emission tomography emulation from decimated high statistics: A clinical validation study. *Med Phys.* (2019) Jun;46(6):2638-2645. doi: 10.1002/mp.13517. PMID: 30929270.
- <sup>55</sup> Pisano, E. D. et al. Diagnostic performance of digital versus film mammography for breast-cancer screening. *N Engl J Med.* (2005). 353, 1773–1783
- <sup>56</sup> National Cancer Institute Breast Cancer Surveillance Consortium website. Distribution of key variables: BI-RADS breast density. (2014).
- <sup>57</sup> Song, D., Man, X., Jin, M., Li, Q., Wang, H. and Du, Y. A Decision-Making Supporting Prediction Method for Breast Cancer Neoadjuvant Chemotherapy. *Front. Oncol.* (2021).10:592556. doi: 10.3389/fonc.2020.5925566
- <sup>58</sup> Michalski, M. H., & Chen, X. Molecular imaging in cancer treatment. *EJNMMI.* (2011). 38(2), 358–377. <https://doi.org/10.1007/s00259-010-1569-z>
- <sup>59</sup> Masood, S. Neoadjuvant chemotherapy in breast cancers. *Women's health (London, England)* vol. 12,5 (2016): 480-491. doi:10.1177/1745505716677139
- <sup>60</sup> Ulaner, Gary A. PET/CT for Patients With Breast Cancer: Where Is the Clinical Impact?. *AJR.* 213.2 (2019): 254-265.
- <sup>61</sup> Vugts, G., Maaskant-Braat, A. J. G., Nieuwenhuijzen, G. A. P., et. al. Patterns of Care in the Administration of Neo-adjuvant Chemotherapy for Breast Cancer. A Population-Based Study. *Breast J.* (2016). 22(3), 316–321. doi:10.1111/tbj.12568
- <sup>62</sup> Rousset, O., Rahmim, A., Alavi, A., & Zaidi, H. Partial volume correction strategies in PET. (2007). *PET Clin.*, 2(2), 235-249
- <sup>63</sup> Hoetjes, N. J., van Veldenm F. H. P., Hoekstra, O. D., et al. Partial volume correction strategies for quantitative FDG PET in oncology. *Eur. J. Nucl. Med. Mol. Imaging* (2010). 37, 1679–1687.
- <sup>64</sup> Cañadas, M., Embid, M., Lage, E., Desco, M., Vaquero, J. J., and Pérez, J. M. NEMA NU 4-

---

2008 Performance Measurements of Two Commercial Small-Animal PET Scanners: ClearPET and rPET-1. *IEEE Trans. Nucl. Sci.* (2011). vol. 58, no. 1, pp. 58-65. doi: 10.1109/TNS.2010.2072935.

<sup>65</sup> Shkumat, N. A. *et al.* Investigating the limit of detectability of a positron emission mammography device: A phantom study. *Med. Phys.* (2011). **38**, 5176–5185

<sup>66</sup> Stiles, J., Baldassi, B., Bubon, O., *et. al.* Evaluation of a High-Sensitivity Organ-Targeted PET Camera. *Sensors.* (2022). 22(13):4678.

<sup>67</sup> Hallen, P., Schug, D. & Schulz, V. Comments on the NEMA NU 4-2008 Standard on Performance Measurement of Small Animal Positron Emission Tomographs. *EJNMMI Phys.* (2020). **7**

<sup>68</sup> Luo, W., Anashkin, E. & Matthews, C. G. Performance evaluation of a PEM scanner using the NEMA NU 4-2008 small animal PET standards. *IEEE Trans. Nucl. Sci.* (2010). **57**, 94–103

<sup>69</sup> Rose A. Vision: human and electronic. *Opt. Phys. Eng.* (1973) New York: Plenum Press

<sup>70</sup> Øen, S. K., Aasheim, L. B., Eikenes, L. & Karlberg, A. M. Image quality and detectability in Siemens Biograph PET/MRI and PET/CT systems—a phantom study. *EJNMMI Phys.* (2019). **6**, 1–16

<sup>71</sup> National Electrical Manufactureres Association. NEMA NU 2-2018. Performance Measurements of Positron Emission Tomographs. (2018).

<sup>72</sup> Morimoto-Ishikawa, D., Hanaoka, K., Watanabe, S. *et al.* Evaluation of the performance of a high-resolution time-of-flight PET system dedicated to the head and breast according to NEMA NU 2-2012 standard. *EJNMMI Phys.* (2022). **9**, 88

<sup>73</sup> Van Sluis, J. *et al.* Performance characteristics of the digital biograph vision PET/CT system. *J. Nucl. Med.* (2019). **60**, 1031–1036

<sup>74</sup> National Electrical Manufactureres Association. NEMA Standards Publication NU 1-2007. 1–39 (2007).

<sup>75</sup> Nuclear Medicine Committee. Computer-Aided Scintillation Camera Acceptance Testing.

---

(1982). 1–44.

<sup>76</sup> Hartevelde, A. A., Meeuwis, A. P., Disselhorst, J. A., Slump, C. H., Oyen, W. J., Boerman, O. C., & Visser, E. P. Using the NEMA NU 4 PET image quality phantom in multipinhole small-animal SPECT. *J. Nucl. Med.* (2011). 52(10), 1646–1653. <https://doi.org/10.2967/jnumed.110.087114>

<sup>77</sup> Prieto, E et al. Evaluation of spatial resolution of a PET scanner through the simulation and experimental measurement of the recovery coefficient. *Comput. Biol. Med.* vol. 40,1 (2010): 75–80. doi:10.1016/j.combiomed.2009.11.002

<sup>78</sup> Keramida, G., et al. The appropriate whole-body index on which to base standardized uptake value in 2-deoxy-2-[18F] fludeoxyglucose PET. *Brit. J. Radiol.* (2015). 88.1052: 20140520.

<sup>79</sup> Kuerer, H. M., et al. A Clinical Feasibility Trial for Identification of Exceptional Responders in Whom Breast Cancer Surgery Can Be Eliminated Following Neoadjuvant Systemic Therapy. *Ann. Surg.* (2018). vol. 267,5: 946-951. doi:10.1097/SLA.0000000000002313

<sup>80</sup> Soret, M., Bacharach, S. L. & Buvat, I. Partial-volume effect in PET tumor imaging. *J. Nucl. Med.* (2007). 48, 932–945

<sup>81</sup> Cysouw, M. C. F. et al. Impact of partial-volume correction in oncological PET studies: a systematic review and meta-analysis. *Eur. J. Nucl. Med. Mol. Imaging* (2017). 44, 2105–2116

<sup>82</sup> Snyder, D. L., Miller, M. I., Thomas, L. J. & Politte, D. G. Noise and Edge Artifacts in Maximum-Likelihood Reconstructions for Emission Tomography. *IEEE Trans. Med. Imaging* (1987). 6, 228–238

<sup>83</sup> Goertzen, A. L. et al. NEMA NU 4-2008 comparison of preclinical PET imaging systems. *J. Nucl. Med.* (2012). 53, 1300–1309

<sup>84</sup> Srinivas, Shyam M et al. A recovery coefficient method for partial volume correction of PET images. *Ann. Nucl. Med.* vol. 23,4 (2009): 341-8. doi:10.1007/s12149-009-0241-9

- 
- 85 Meechai T., Tepmongkol, S., Pluempitiwiriyaewej, C. Partial-volume effect correction in positron emission tomography brain scan image using super-resolution image reconstruction. *Br. J. Radiol.* (2015). 88:20140119.
- <sup>86</sup> Vaidya, J.S., Massarut, S., Vaidya, H.J., Alexander, E.C., Richards, T., Caris, J.A., Sirohi, B., Tobias, J.S. Rethinking neoadjuvant chemotherapy for breast cancer. *BMJ.* (2018). Jan 11;360:j5913. doi: 10.1136/bmj.j5913. PMID: 29326104.
- <sup>87</sup> Sugawara, Y., Zasadny, K. R., Neuhoff, A. W., and Wahl, R. L. Reevaluation of the Standardized Uptake Value for FDG: Variations with Body Weight and Methods for Correction. *Radiology* (1999). 213:2, 521-525
- <sup>88</sup> Beaulieu, Sylvain, et al. SUV varies with time after injection in 18F-FDG PET of breast cancer: characterization and method to adjust for time differences. *J. Nucl. Med.* 44.7 (2003): 1044-1050
- <sup>89</sup> Macdonald L.R., Hippe D.S., Bender L.C., Cotter E.W., Voria P.R., Hallam P.S., Wang C.L., Haseley D.R., Kelly M.M., Parikh J.R., et al. Positron emission mammography image interpretation for reduced image count levels. *J. Nucl. Med.* (2016). 57:348–354. doi: 10.2967/jnumed.115.165787
- <sup>90</sup> Boellaard R., et al. FDG PET/CT: EANM procedure guidelines for tumour imaging: Version 2.0. *Eur. J. Nucl. Med. Mol. Imaging.* (2015). 42:328–354. doi: 10.1007/s00259-014-2961-x.
- <sup>91</sup> Pestalozzi, Bernhard C., et al. Distinct clinical and prognostic features of infiltrating lobular carcinoma of the breast: combined results of 15 International Breast Cancer Study Group clinical trials. *J. Clin. Oncol.* (2008). 26.18 3006-3014.
- <sup>92</sup> Mukhtar, R.A., Hoskin, T.L., Habermann, E.B. et al. Changes in Management Strategy and Impact of Neoadjuvant Therapy on Extent of Surgery in Invasive Lobular Carcinoma of the Breast: Analysis of the National Cancer Database (NCDB). *Ann. Surg. Oncol.* (2021). 28, 5867–5877 <https://doi.org/10.1245/s10434-021-09715-3>
- <sup>93</sup> Jung, Na Young et al. Associations between the standardized uptake value of (18)F-FDG PET/CT and the prognostic factors of invasive lobular carcinoma: in comparison with invasive ductal carcinoma. *World J. Surg. Oncol* (2015). vol. 13 113. doi:10.1186/s12957-015-0522-9

---

<sup>94</sup> Fujii, Takaaki, et al. Clinical significance of <sup>18</sup>F-FDG-PET in invasive lobular carcinoma. *Anticancer Res.* (2016). 36.10 5481-5485.

<sup>95</sup> Fujii, Takaaki et al. Clinicopathological Features of Cases with Primary Breast Cancer not Identified by 18F-FDG-PET. *Anticancer Res.* (2016). vol. 36,6 3019-22.

<sup>96</sup> Sanli, Yasemin et al. Increased FDG uptake in breast cancer is associated with prognostic factors. *Ann. Nucl. Med.* (2012). vol. 26,4: 345-50. doi:10.1007/s12149-012-0579-2

<sup>97</sup> Alavi, A., Werner, T. J., Høilund-Carlsen, P. F. & Zaidi, H. Correction for Partial Volume Effect Is a Must, Not a Luxury, to Fully Exploit the Potential of Quantitative PET Imaging in Clinical Oncology. *Mol. Imaging Biol.* (2018). 20, 5–7